An infrared desert dust index for the Along-Track Scanning Radiometers

Remote Sensing of Environment 116 (2012) 159–176

Contents lists available at ScienceDirect

Remote Sensing of Environment

journal homepage: www.elsevier.com/locate/rse

An infrared desert dust index for the Along-Track Scanning Radiometers

E.J. Good [a,*], X. Kong [a], O. Embury [b], C.J. Merchant [b], J.J. Remedios [a]

[a] Earth Observation Science Group, Department of Physics and Astronomy, University of Leicester, United Kingdom
[b] School of GeoSciences, The University of Edinburgh, United Kingdom

ARTICLE INFO

Article history:
Received 27 August 2009
Received in revised form 4 June 2010
Accepted 27 June 2010
Available online 28 July 2011

Keywords:
Saharan dust
Tropospheric aerosol
Sea surface temperature
Along-Track Scanning Radiometer
Thermal remote sensing

ABSTRACT

A new aerosol index for the Along-Track Scanning Radiometers (ATSRs) is presented that provides a means to detect desert dust contamination in infrared SST retrievals. The ATSR Saharan dust index (ASDI) utilises only the thermal infrared channels and may therefore be applied consistently to the entire ATSR data record (1991 to present), for both day time and night time observations. The derivation of the ASDI is based on a principal component (PC) analysis (PCA) of two unique pairs of channel brightness temperature differences (BTDs). In 2-D space (i.e. BTD vs BTD), it is found that the loci of data unaffected by aerosol are confined to a single axis of variability. In contrast, the loci of aerosol-contaminated data fall off-axis, shifting in a direction that is approximately orthogonal to the clear-sky axis. The ASDI is therefore defined to be the second PC, where the first PC accounts for the clear-sky variability. The primary ASDI utilises the ATSR nadir and forward-view observations at 11 and 12 μm (ASDI2). A secondary, three-channel nadir-only ASDI (ASDI3) is also defined for situations where data from the forward view are not available. Empirical and theoretical analyses suggest that ASDI is well correlated with aerosol optical depth (AOD: correlation r is typically >0.7) and provides an effective tool for detecting desert mineral dust. Overall, ASDI2 is found to be more effective than ASDI3, with the latter being sensitive only to very high dust loading. In addition, use of ASDI3 is confined to night time observations as it relies on data from the 3.7 μm channel, which is sensitive to reflected solar radiation. This highlights the benefits of having data from both a nadir- and a forward-view for this particular approach to aerosol detection.

1. Introduction

Infrared satellite observations of sea surface temperature (SST) have become essential for many modern day applications in meteorology, climatology and oceanography. Several data sets are now made routinely available to users, for example from the Along-Track Scanning Radiometers (ATSRs; ESA, 2002), Advanced Very High Resolution Radiometers (AVHRRs; Kilpatrick et al., 2001) and the Spinning Enhanced Infrared and Visible Radiometer (SEVIRI; Brisson et al., 1998). The accuracy of these data, which are estimated from satellite top of atmosphere (TOA) radiance observations, is dependent upon several factors, such as the radiometric accuracy of the sensor, the retrieval algorithm, and the ability to correctly identify cloud. A number of studies have shown that SST retrievals may be biased by up to several tenths of a degree in the presence of tropospheric mineral dust aerosol (Donlon & Robinson, 1998; Merchant et al., 2006; Noyes et al., 2006; Vazquez-Cuervo et al., 2004). An area particularly affected by this problem is the Atlantic Ocean between West Africa and the Caribbean, where dust is lofted and blown west from the Sahara. These so-called Saharan dust events may occur at any time during the year, but are strongest and most frequent during the northern hemisphere summer months (Carlson & Prospero, 1972). Satellite SST observations where the dust loading is very high are often incorrectly flagged as cloud. However, apparently cloud-free, dust-contaminated SST retrievals are still prevalent enough to warrant the implementation of a specific strategy to either remove these observations, or develop a bias correction method, as the magnitude of the bias induced by the aerosols may exceed the accuracy requirement for many SST applications.

The objective of this study is to develop a method to detect tropospheric mineral dust in ATSR observations over the oceans that may cause SST biases.

Aerosol detection methods using visible wavelengths are well established (e.g. Brindley & Ignatov, 2006; Grey et al., 2006; Tanré et al., 1997; Thomas et al., 2007; Veefkind & de Leeuw, 1998) and have been used previously to detect the presence of aerosols in infrared SST data (e.g. Noyes et al., 2006; Vazquez-Cuervo et al., 2004). However, these data have two main limitations for this type of application. Firstly, the aerosol data are restricted to day time observations only, whereas SSTs are retrieved both at night and during the day. Secondly, the effects of aerosol at infrared wavelengths are not uniquely determined from observation of aerosol effects at visible wavelengths. For example, small-particle aerosols, such as those originating from biomass burning, are often readily detected at visible wavelengths,

* Corresponding author at: Met Office Hadley Centre, Exeter, United Kingdom.
E-mail address: elizabeth.good@metoffice.gov.uk (E.J. Good).

0034-4257/$ – see front matter © 2011 Elsevier Inc. All rights reserved.
doi:10.1016/j.rse.2010.06.016

but usually have very little effect on retrieved SSTs. Given these limitations, it is desirable to develop a method of dust detection for the ATSRs that uses only infrared data that can be used both during the day and at night.

Aerosol detection using infrared satellite observations has been reported elsewhere in the literature, for example by Merchant et al. (2006), Brindley and Russell (2006) and Thomas et al. (2009). In this study, we adopt the approach of Merchant et al. (2006), who developed a Saharan dust index (SDI) for use over oceans using the thermal channels of the SEVIRI using a principal component analysis (PCA). This paper describes the development and evaluation of an ATSR equivalent to the SDI, which is hereafter referred to as the ATSR SDI, or ASDI. We begin in Section 2 by describing the study area and data sets used in this analysis and outlining Merchant et al.'s (2006) technique. In Section 3, the effects of Saharan dust on ATSR TOA infrared observations are investigated both theoretically and empirically. Using the results of these experiments, the ASDI is defined in Section 4. In Section 5, we explore the behaviour of the ASDI when applied to empirical data, and validate the dust index with other independent aerosol data sets.

2. Study area and data sets

The objective of this study is to define the ASDI, a Saharan dust index that uses only infrared ATSR observations. Key to this process is the use of SEVIRI SDI data, which are used as an independent measure of aerosol in the ATSR data and as a basis for defining the ASDI. Using SDI data in this way is convenient because 1) SDI is a thermal infrared dust index so should be indicative of aerosol effects in the infrared, and 2) being on a geostationary platform, SEVIRI observations are frequent and therefore provide the opportunity to obtain a good temporal match with the ATSR overpass time where empirical investigations are performed.

The main area chosen for this study lies between 0° and 30°N and 50° and 0°W. This area was selected firstly, because strong Saharan dust events occur frequently in the region, and secondly, because this area falls within the SEVIRI field of view (FOV) at view zenith angles for which reliable SDI can be obtained. The analysis carried out here is mostly based on data for the year 2005. The following sections describe the ATSR and SEVIRI data used in this study.

2.1. The Along-Track Scanning Radiometers

The ATSR series to date comprises three instruments. The first, ATSR-1, was launched in 1991 on board the European Space Agency's (ESA) polar-orbiting European Remote Sensing satellite-1 (ERS-1). This was followed by the launch of ATSR-2 in 1995 on board ERS-2, and most recently, the Advanced ATSR (AATSR) in 2002 on ESA's Envisat platform. At the time of writing, the AATSR is still fully operational.

The primary objective of the ATSR missions is to provide accurate SST retrievals on a global scale. All ATSR instruments share a common design that facilitates SST retrieval with an accuracy that is currently unmatched by any other space borne sensor. A unique feature is the conical scan mechanism that allows the surface of the earth to be viewed at both nadir and approximately 55° from zenith, enabling an improved atmospheric correction. The ATSR instruments also have exceptional infrared radiometric accuracy ($\ll$0.1 K) and stability (specified drift of the on board calibration system is less than 0.03 K over a nominal sensor lifetime of 5 years). This is achieved through the use of two onboard calibration black bodies and actively-cooled detectors (Llewellyn-Jones et al., 2001; Mason, 1991; Smith et al., 2001). All the ATSR instruments carry three infrared channels, at approximately 3.7, 11 and 12 μm for SST retrieval, together with a channel at 1.6 μm for cloud detection. ATSR-2 and AATSR also have additional visible channels at 0.56, 0.66 and 0.87 μm for remote sensing of chlorophyll and vegetation, and for cloud detection over land.

Owing to these design features, the orbit stability and temporal consistency of the ERS and Envisat platforms, and the existence of sufficient overlap periods, the ATSR mission provides a unique opportunity to generate a global long-term, high accuracy, homogeneous SST record independently of *in situ* observations. This is the objective of the ATSR Reanalysis for Climate (ARC) project, which aims 'to reduce regional biases in retrieved SST to less than 0.1 K for all global oceans, while creating a homogenous record that is stable in time to within 0.05 K decade^{-1}' (Merchant et al., 2008). The ASDI developed here was formulated within the framework of the ARC project and will be used to identify the presence of dust in the ARC SST data sets and to flag SST retrievals that may be biased as a result.

The ATSR data used in this study were obtained from the NERC (Natural Environment Research Council) Earth Observation Data Centre (NEODC: see http://www.neodc.rl.ac.uk/). We use Level 1b 1-km gridded brightness temperature (BT) data, processed using software developed at the University of Leicester. The geolocation (i.e. pixel to geographical latitude and longitude) of these data has been performed as in the AATSR Frequently Asked Questions (FAQ), Appendix A (document ref: AEP.REP.001 (2005)—download from http://envisat.esa.int/instruments/aatsr/faq/AATSR/FAQ/issue1.pdf). For each ATSR data set used here, an alignment correction has been applied following Corlett (2009), where the forward view is shifted relative to the nadir view by −2 pixels in the along track direction, and +2 pixels in the across-track direction. For AATSR, 0.2 K has been added to both forward and nadir 12 μm BTs following the work of Nightingale and Birks (2004), who report a BT deficit of approximately this magnitude, which is likely to be a result of an incorrect pre-launch measurement of the spectral response function (Smith, 2007). (Note: this problem is unique to AATSR; ATSR-1 and ATSR-2 are not affected).

Operational ATSR SST data are not used in this study. However, the effects on SST retrievals are predicted from the results of the radiative transfer modelling by applying the operational retrieval coefficients for 2005, specified in the file ATS_SST_AXVIEC20051205_102103_20020101_000000_20200101_000000.N1 (download from http://earth.esa.int/services/auxiliary_data/aatsr/).

2.1.1. ATSR SST retrievals

ATSR SST estimates, x, are retrieved using a linear function of top of atmosphere brightness temperatures (BT—this is the equivalent black body temperature that produces the observed channel radiances):

$$x = a_0 + \sum_{i=1}^{n} a_i y_i \quad (1)$$

where n is the number of observations used, y_i is the BT obtained from channel i (either from the nadir-view only or both the forward- and nadir-views) and a_0 and a_i are retrieval coefficients. Four different SST retrievals, can be performed: dual three-channel (D3), which use all three thermal infrared channels from both views, nadir three-channel (N3), which again uses all three channels but only in the nadir-view, and the dual and nadir two-channel coefficients (D2 and N2), which do not include the 3.7 μm channel and are used during the day when the 3.7 μm channel is contaminated by reflected solar radiation. See Table 1 for terminology.

The retrieval coefficients are derived theoretically using a radiative transfer model (RTM), by regressing the simulated BTs against the SSTs used in the model for a large number of atmospheric scenarios (Merchant et al., 1999; Závody et al., 1995). Previous validation of the operational ATSR SST retrieval against in situ observations suggests that most of the data meet the required 0.3 K (one standard deviation) accuracy under cloud-free conditions (Corlett et al., 2006; Noyes et al., 2006; O'Carroll et al., 2006; O'Carroll et al., 2008). Following the work

Table 1
Definition of variables in this article.

Term	Definition
n37	ATSR nadir 3.7 μm BT
f37	ATSR forward 3.7 μm BT
n11	ATSR nadir 11 μm BT
f11	ATSR forward 11 μm BT
n12	ATSR nadir 12 μm BT
f12	ATSR forward 12 μm BT
N2	Nadir two-channel ATSR SST retrieval
N3	Nadir three-channel ATSR SST retrieval
D2	Dual-view two-channel ATSR SST retrieval
D3	Dual-view three-channel ATSR SST retrieval
BT_{clear}	RTTOV-modelled clear-sky BT
$BT_{aerosol}$	RTTOV-DISORT-modelled non clear-sky BT (with aerosol loading)
ΔBT	$BT_{aerosol} - BT_{clear.}$, or change in BT due to aerosol with respect to clear-sky
SST_{clear}	SST retrieved using BT_{clear} only
$SST_{aerosol}$	SST retrieved using $BT_{aerosol}$ only
ΔSST	$SST_{aerosol} - SST_{clear.}$, or change in retrieved model SST due to aerosol with respect to clear-sky

of Merchant et al. (1999), the operational SST retrievals were made robust to stratospheric aerosol. However, there is evidence to suggest that the retrievals may still be significantly biased in the presence of tropospheric mineral dust aerosol (Noyes et al., 2006). The dual-view SST retrievals appear to be more robust to these effects than the nadir-view only retrievals, which may be cold-biased by several tenths of a degree. In contrast, the results of Noyes et al. (2006) suggest that the dual-view retrievals can be positively biased in the presence of Saharan dust by up to a few tenths of a degree.

2.2. SEVIRI Saharan dust index

The dust detection method developed in this study for the ATSR instruments is based on the SEVIRI SDI, described by Merchant et al. (2006). Saharan dust has been found to induce negative biases in SEVIRI SST retrievals, so the SDI was developed to i) provide a method of detecting the presence of Saharan dust in SEVIRI observations, and ii) bias correct SEVIRI SST retrievals using an empirical correction scheme. The SEVIRI SDI is used in this study to investigate the effects of Saharan dust aerosol on ATSR data both theoretically and empirically. The description below is based on Merchant et al. (2006) and references therein.

The SEVIRI is the imaging sensor deployed on the Meteosat platform, which is the operational geostationary satellite at 0° longitude. Full-disc images covering the Atlantic Ocean, Europe, South America and Africa are acquired every 15 min. Like the ATSR, SEVIRI is an imaging radiometer with channels operating in the visible and thermal infrared. SST retrievals are performed using the channels at 10.8 and 12 μm over the Eastern Atlantic and the Western Indian Ocean, with an accuracy of better than 1 K.

The SDI is calculated from the SEVIRI thermal channels, and although correlated with aerosol optical depth (AOD), it is not exactly equivalent as it is also sensitive to the height of the aerosol. In practice, an operational SDI is derived from four SEVIRI channel BTs:

$$SDI = 0.532(BT_{3.9} - BT_{8.7} + 0.933) - 0.847(BT_{11} - BT_{12} - 1.144) \quad (2)$$

where the subscripts 3.9, 8.7, 11 and 12 correspond to the SEVIRI channels at these wavelengths (in μm). Owing to the use of the 3.9 μm channel, SDI is only calculated for night time observations as this channel can be contaminated by reflected solar light during the day. A compositing technique using the most recent value over the previous 24 h allows SDI values to be estimated for daytime also, but with increased error compared to night time, because of the movements of dust during the day. The SDI is scaled to correspond approximately with visible AOD for Saharan Dust and is seen to range from approximately −3 to +6, where more positive values generally indicate more dust. Experience shows that values greater than 0.2 reliably indicate the presence of dust (this corresponds approximately to a visible AOD of 0.2).

The SEVIRI data used in this study are provided by the EUMETSAT Ocean and Sea Ice Satellite Application Facility. The data used here are the TOA BT data; the SDI data presented in this study correspond to zenith angles of ≤60° and have been derived using Eq. (2).

3. Effect of dust on ATSR observations

Before we can develop a dust detection strategy for the ATSRs, we must first understand how dust affects the TOA observations. A number of previous studies, some of which are mentioned in more detail further below, report the effects of mineral dust on satellite thermal infrared radiances near to the ATSR channels at 11, 12 and 3.7 μm. Most of these studies have taken a theoretical approach to estimate the change in TOA signal when aerosol is present, using a radiative transfer model to simulate BTs for various dust layer AOD and heights. These previous studies conclude that mineral dust aerosol depresses the TOA signal, with wavelengths around 11 μm most significantly affected, followed by 12 μm, with the smallest effect observed at around 3.7 μm. Aerosol effects on TOA BTs are also found to increase with increasing dust altitude.

For example, Pierangelo et al. (2004) used aerosol properties reported by Hess et al. (1998) for transported mineral dust to simulate the effects on the Aqua-Advanced Infrared Radiation Sounder (AIRS) infrared channels. They report an increase in the BT depression due to dust from about 2 to10 K in the 11–12 μm region and <2 to 6 K at 3.7 μm when increasing the AOD at 10 μm from 0.75 to 2.5 for a dust layer at 2400 m. Pierangelo et al. (2004) also report that increasing the dust altitude from 800 to 4000 m in their simulations increases the BT deficit by a factor of three to four, with the altitude effects at longer wavelengths being stronger than those at shorter wavelengths. Merchant et al. (2006) also use the Hess et al. (1998) aerosol properties, together with a second set derived from data reported by Highwood et al. (2003), to predict the effects of Saharan dust on SEVIRI thermal channel observations. For an aerosol layer with 10 μm AOD of 1.0 at 2–3 km height, they predict mean BT deficits due to aerosol of about 5 to 6 K at 11 μm, 3.5 to 5 K at 12 μm, and 2.5 to 3 K at 3.9 μm. They also find that increasing the base height of a 1-km layer of dust with 10 μm AOD of 0.5 from 0 to 4 km increases the BT deficit by a factor of about three to four at 11 and 12 μm, and a factor of 1.5 at 3.9 μm.

For the ATSR instruments, Dundas (1997) used a radiative transfer model to simulate the effects of mineral dust on the ATSR-1 and -2, showing enhanced effects in the forward view with respect to the nadir. Similar results are also reported by Noyes (2005), who uses a combination of simulated and observed AATSR BTs to estimate the depression due to tropospheric mineral dust aerosol in the Caribbean. In the Noyes (2005) study, the BT deficit in the forward view is found to be two to three times larger than that in the nadir view.

In this study, the effects of Saharan dust on ATSR BTs are examined both theoretically and empirically. First, a radiative transfer model is used to simulate both dust-contaminated and dust-free BTs for a given set of atmospheric and surface conditions. The change in BT due to aerosol for a particular atmospheric scenario is defined as the difference between the dust and dust-free simulations. Secondly, these results are verified using empirically-derived estimates of the BT depression due to dust. In both cases, the change in BT is examined as a function of SEVIRI SDI as an independent measure of dust.

3.1. Dust simulations

3.1.1. Radiative transfer model

Following the approach of Merchant et al. (2006) in developing their SEVIRI SDI, we use a modified version of the fast forward model

RTTOV (version 8.7; Saunders et al., 1999; Saunders & Pascal, 2005) to calculate TOA BTs. The standard RTTOV model calculates instrument and channel specific transmittances for an input atmospheric state (profile of temperature, water vapour etc.); it then solves the radiative transfer equation (RTE) using an absorption-only approximation to give clear-sky radiances. Merchant et al. (2006) replaced the standard RTE solver with a delta-Eddington approximation allowing simple scattering calculations to be performed. In this study, the discrete ordinates or DISORT (Stamnes et al., 1988) code is used as the solver due to its greater numerical accuracy.

Optical properties of aerosols are taken from two sources for comparison: the transported mineral aerosol from the Optical Properties of Aerosol and Cloud (OPAC—Hess et al., 1998), and the aerosol properties derived from observations at the Dakhla AERONET site (23.72°N, 15.95°W) reported by Highwood et al. (2003) using Mie theory (the Mie calculations come courtesy of J. Haywood and A. O'Carroll at the Met Office, and are hereafter referred to as the 'Haywood' aerosol properties). Both sets of aerosol optical properties are shown in Fig. 1. The extinction coefficient (β), shown normalised to 1.0 at 10 μm, is used to scale the AOD to the value appropriate for a given instrument/channel. The single scattering albedo (ω), the ratio of scattering coefficient to extinction coefficient, indicates the probability of a scattering interaction. Finally the asymmetry parameter (g) is the first moment of the scattering phase function and indicates the relative amounts of forward and backward scattering.

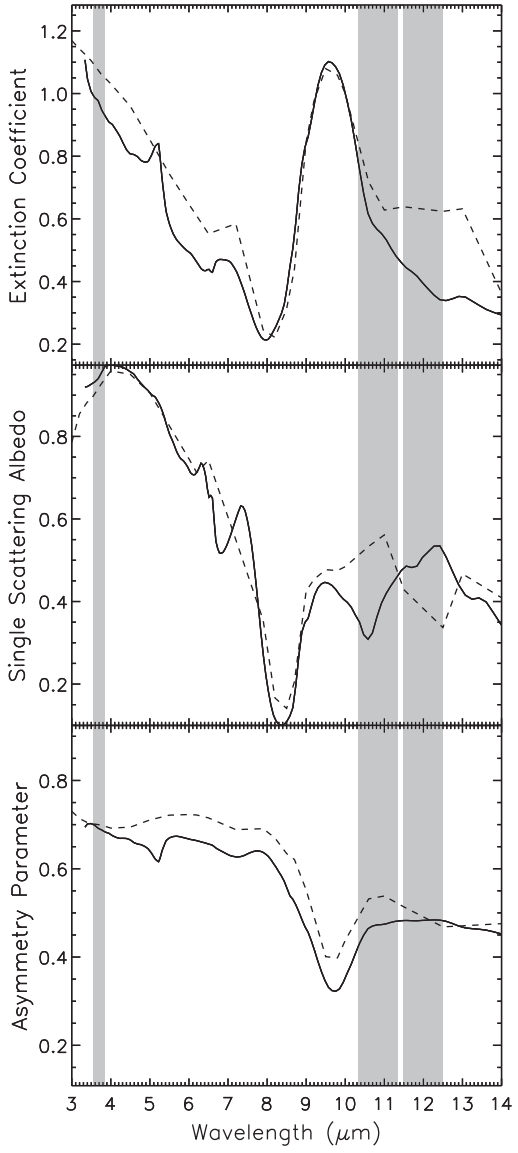

Fig. 1. Variation in aerosol parameters with wavelength for the Haywood (solid lines) and OPAC (dashed lines) data sets. Also shown are the ATSR thermal channel wavebands (grey shading).

The model is run for a prescribed set of atmospheric and surface conditions, together with a defined aerosol layer AOD and height information. The output consists of both clear-sky and aerosol-contaminated BTs for each atmospheric/surface scenario. The change in BT, or ΔBT, due to aerosol is defined to be the aerosol-contaminated BT ($BT_{aerosol}$) minus the clear-sky BT (BT_{clear}) for that scenario, such that a negative ΔBT indicates that aerosol reduces the observed BT (Table 1).

The atmospheric and surface conditions used in the model simulations are defined from the profile data set of Merchant et al. (1999) used for generating ATSR SST coefficients. The complete data set consists of 1358 profiles derived from the European Centre for Medium Range Weather Forecasts (ECMWF) Re-Analysis (ERA) data set. A subset of 1334 profiles are used in this experiment, corresponding to latitudes between −60 and 60°N. Simulations are performed for near-surface air temperature–SST differences of −3, 0 and +3 K, excluding states where the SST is less than 271.35 K, representing a frozen ocean surface (Merchant et al., 1999). The resulting simulation data set therefore consists of a total of 3898 individual simulation scenarios.

In order to simulate a wide range of dusty conditions, aerosol layers of varying aerosol optical depth (AOD) and height were assigned to each of the 3898 simulations scenarios. In the natural environment, the height of Saharan dust layer over the ocean ranges typically between 1.5 and 4.5 km (Prospero & Carlson, 1972). To account for this variability, the model was run for 1 km dust layers with bases ranging between 1 and 5 km above the surface, with the 10 μm AOD ranging between 0 and 1.0 (where $AOD_{10\mu m} = 0.52.AOD_{0.55\mu m}$, following Highwood et al. (2003)). Although the true vertical distribution of dust may be inhomogeneous, this single 1-km layer scheme was adopted to align this work with that of Merchant et al. (2006) in the development of the SEVIRI SDI, and also to simplify the modelling and subsequent data analysis. Values of 10 μm AOD greater 1.0 ($AOD_{0.55\mu m} \approx 1.92$) are not included in this experiment as pixels with dust loading above this are almost always flagged as cloud, so an infrared dust index designed to flag suspect SST retrievals is not required in this case. (Cloud flagging of pixels with AOD greater than this threshold was confirmed by examining 18 overpasses of AATSR visible AOD (Grey et al., 2006) described in Section 5.2). Both the AOD and aerosol layer heights were generated using a random number generator, with uniform distribution, for each simulation scenario. Model runs were performed for all three ATSR instruments separately, for both the nadir and forward view angles at the centre and edge of the swath (Table 2). SEVIRI thermal channel BTs were also simulated for 0° zenith in order to generate a theoretical SDI with which to compare the ATSR BT simulations. For each instrument, simulations were performed for both sets of aerosol properties (i.e. 'Haywood' and 'OPAC') so that the ATSR BT simulations could be compared directly with the SDI calculated using the same set of aerosol properties.

3.1.2. Results

Figs. 2 and 3 show the effect of AOD and dust layer height, respectively, on AATSR ΔBTs simulated using the Haywood aerosol

Table 2
ATSR zenith angles used in the RTM simulations.

View	View angle (°)	
	Swath centre	Swath edge
Nadir	0.000	21.433
Forward	55.346	52.809

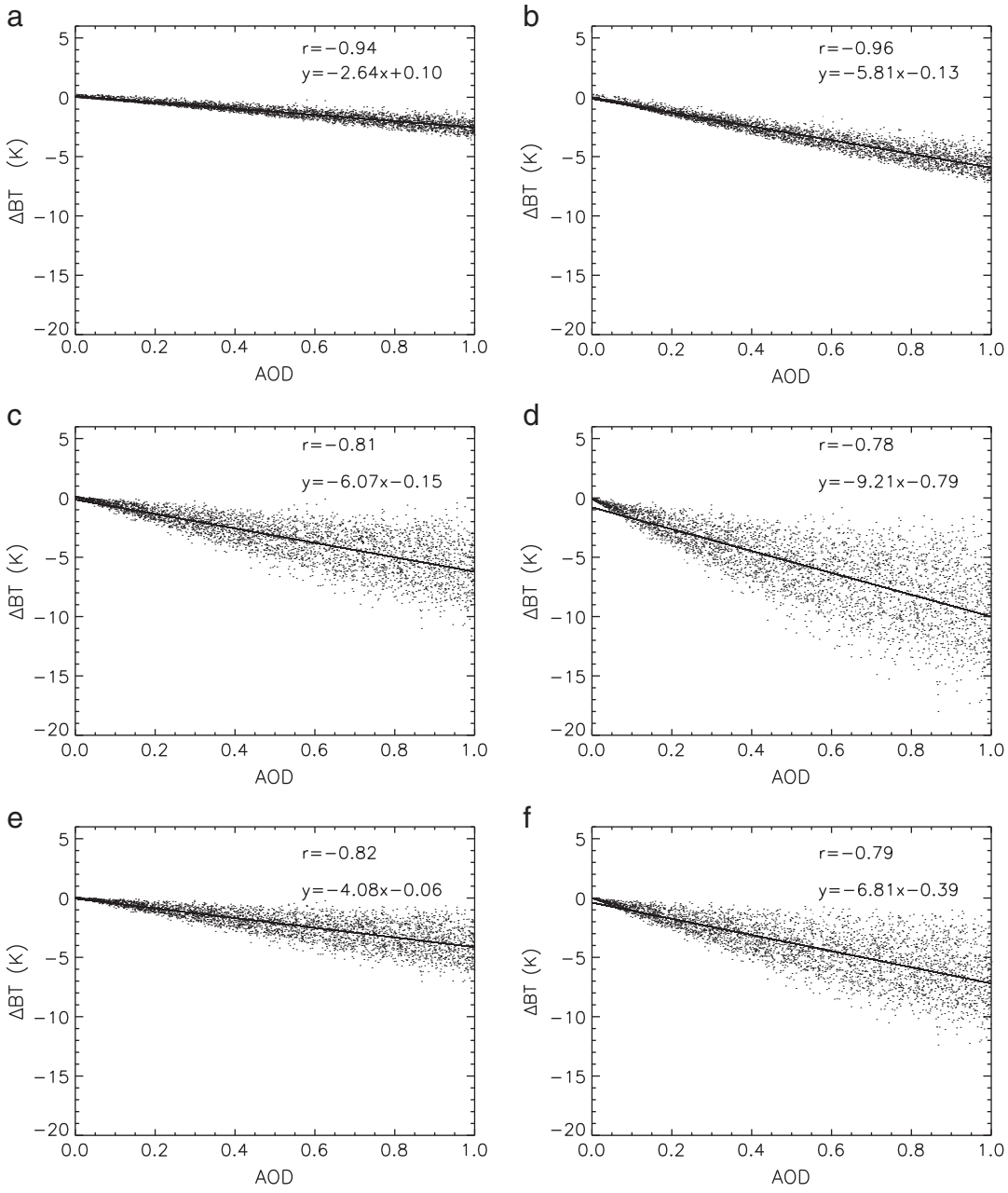

Fig. 2. Simulated change in BT with 10 μm AOD for the AATSR centre of swath for (a) n37, (b) f37, (c) n11, (d) f11, (e) n12 and (f) f12, using the Haywood aerosol parameters. 'r' denotes the Pearson correlation coefficient.

parameters for the centre of swath. The results are consistent with those of previous studies, demonstrating that both the height and AOD have an impact on the magnitude of the ΔBTs, with the largest effect occurring at 11 μm and the smallest at 3.7 μm. As expected, the results also show the effects are enhanced in the AATSR forward view. Although simulations have only been performed for AODs between 0 and 1 the near-linear nature of the ΔBT vs AOD relationship suggests that the regression equations should also approximate well the relationship between these two parameters for values of 10 μm AOD slightly higher than 1. However, the plots in Fig. 2 suggest that ultimately the relationship will break down as the aerosol layer becomes more opaque.

It is also useful to consider any impact of radiometric noise in the ATSR channels in terms of the equivalent change in AOD and height, as this has relevance when implementing the dust index developed later in this study. Owing to the high accuracy and stability of the ATSR instrument, the impact of noise is found to be small. Assuming a maximum radiometric channel noise of 0.1 K (Section 2.1), the equivalent noise levels in 10 μm AOD are between 0.01 and 0.04 (0.55 μm AOD: 0.02 and 0.08), and in aerosol height, 100 to 700 m, depending on the channel and aerosol optical data used.

Regressing the same ΔBTs against the SDI calculated for the corresponding SEVIRI simulations demonstrates how well the SDI captures the variability due to both the aerosol AOD and layer height, particularly for the 11 and 12 μm channels (magnitude of Pearson correlation coefficient $r \geq 0.95$ compared with ~0.8 and 0.4 for AOD and height, respectively: Fig. 4). Almost identical results are obtained for ATSR-1 and -2 (not shown). The rates of change in ΔBT with respect to SDI calculated in this study compare well with the results of Noyes (2005) and Dundas (1997), shown in Table 3. The root mean square (RMS) differences between the different results suggest that the Haywood simulations agree slightly better with the results of

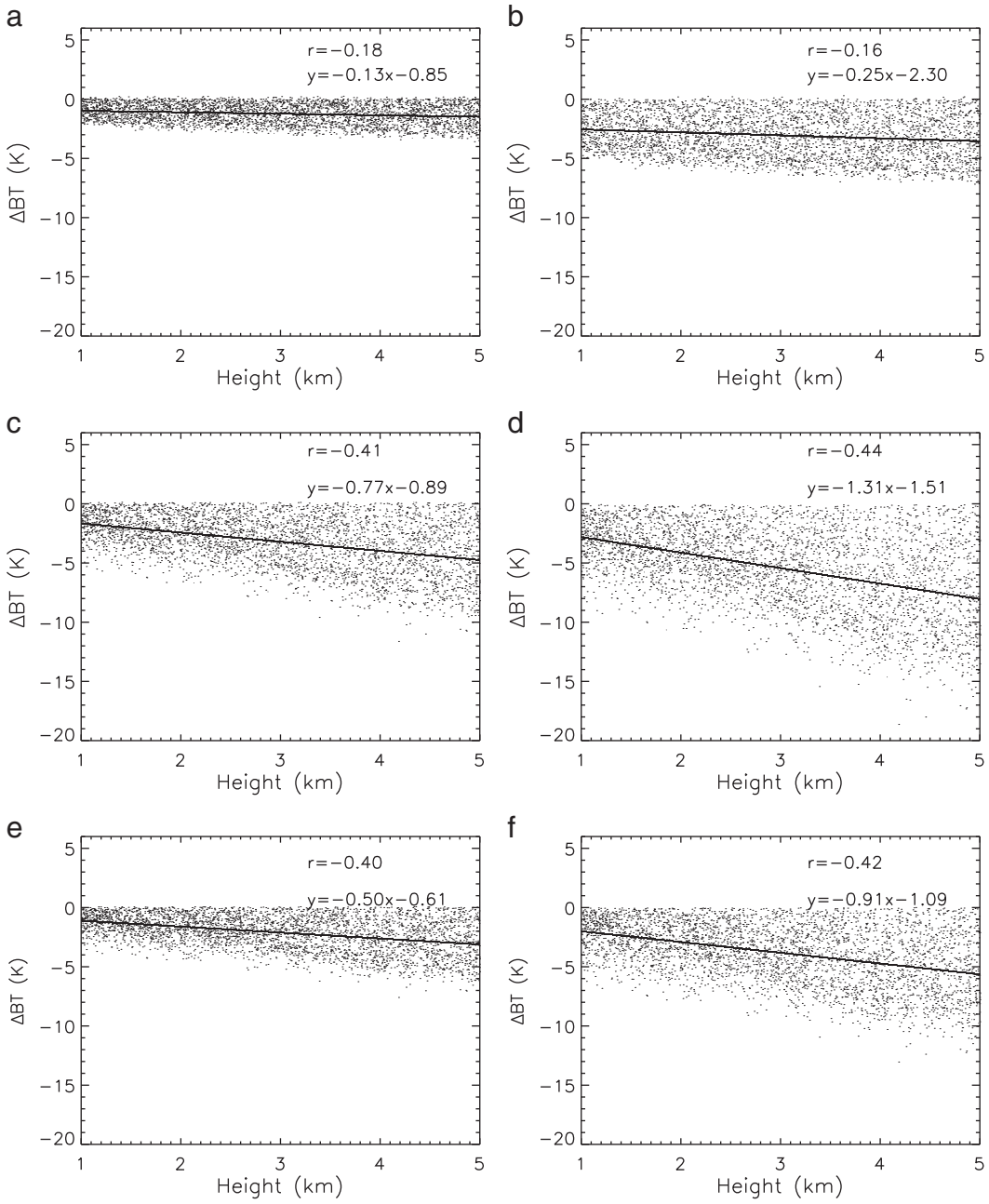

Fig. 3. Simulated change in BT with aerosol layer height (base of 1 km layer) for the AATSR centre of swath for (a) n37, (b) f37, (c) n11, (d) f11, (e) n12 and (f) f12, using the Haywood aerosol parameters. 'r' denotes the Pearson correlation coefficient.

Noyes (2005), while the OPAC simulations are closer to the results of Dundas (1997). However, comparing just the two sets of model runs generated in this study, the rates of change of ΔBT simulated with the different aerosol parameters agree within the standard linear fitting errors for both the centre and edge of ATSR swath (Fig. 5).

The effect that aerosol has on the retrieved ATSR SSTs can also be predicted by applying Eq. (1) to the simulated BTs. Fig. 6 illustrates the simulated SST biases for the AATSR N2, D2 N3 and D3 retrievals. Also shown are the results of Noyes et al. (2006), who estimated the AATSR SST biases due to Saharan dust from the results of a validation experiment in the Caribbean in 2003, where AATSR SSTs have been compared with *in situ* SST data.

Again, the results from the two sets of simulations in this study agree within the estimated uncertainties. Good agreement is also obtained between our results and those of Noyes et al. (2006) for N2 and D3. The agreement for N3 is not as good, but within the uncertainties. However, the agreement for the D2 SSTs is quite poor, with the results of Noyes et al. (2006) showing a strong positive bias, while the Haywood simulations suggest that the bias should be negative. Differences between our results and those of Noyes et al. (2006) may be due to the small sample size (n = 8 and n = 9 for D2 and D3, respectively), and the geographically localised nature of the Noyes et al. (2006) study.

3.2. Dust observations

3.2.1. Approach

In the previous section, the effects of Saharan dust on ATSR BTs have been predicted using an RTM. In this section, we attempt to verify these results empirically, particularly as the modelling results rely on aerosol parameters that may have a high degree of uncertainty.

The methodology adopted for this empirical component of the study is to (1) obtain corresponding AATSR BT and SEVIRI SDI data matched in

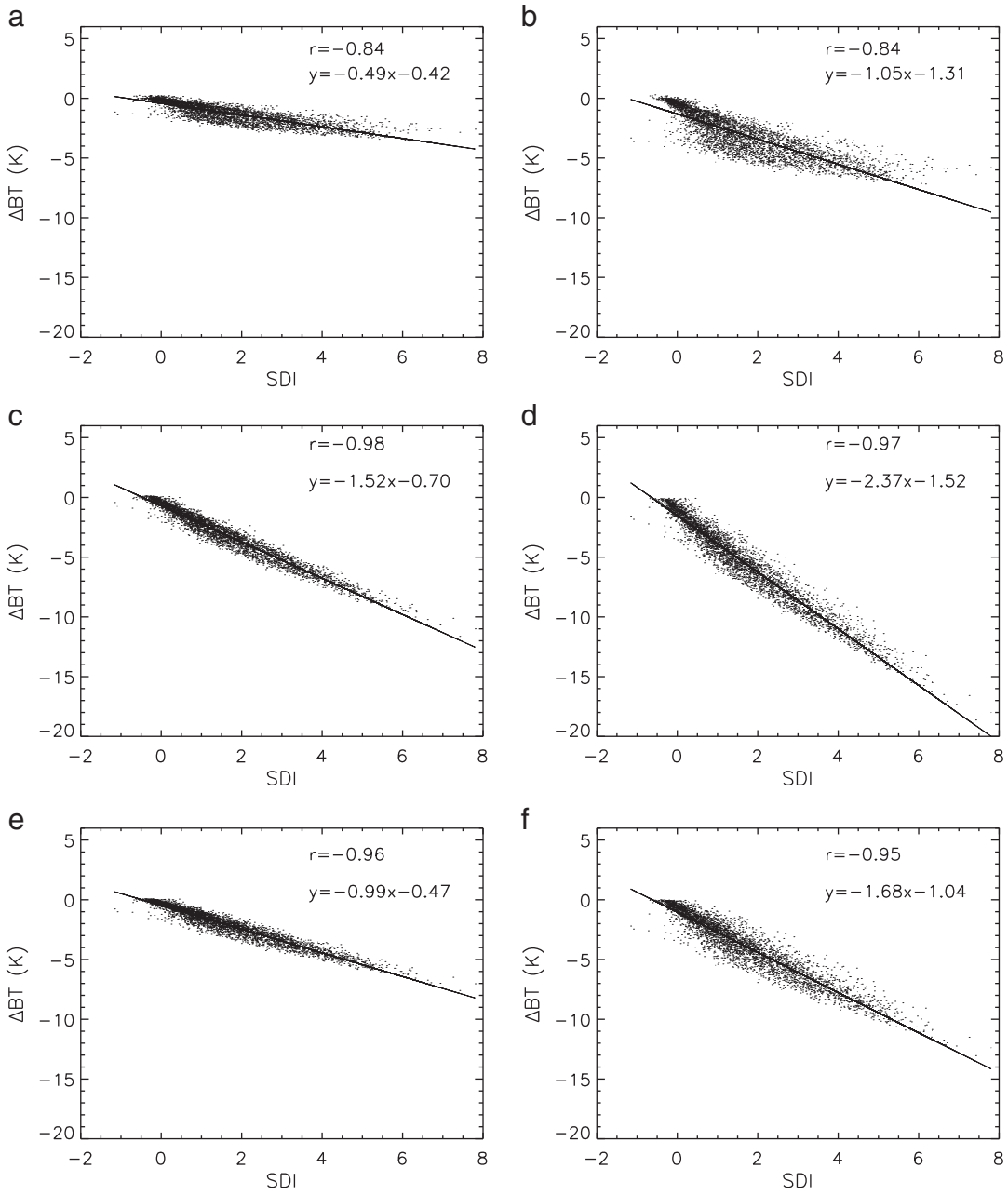

Fig. 4. Simulated change in BT with SDI for the AATSR centre of swath for (a) n37, (b) f37, (c) n11, (d) f11, (e) n12 and (f) f12 using the Haywood aerosol parameters.

both space and time, (2) select some geographical regions where the SDI and its variability is high, and (3) establish the rate of change of ΔBT from the slope of the relationship between the observed AATSR and SEVIRI SDI data. Ideally, we want the empirically-derived BT slopes for each AATSR channel relationship to match those derived theoretically in Section 3.1, giving us confidence in the modelling results.

Table 3
Comparison between the BT deficits due to aerosol obtained in this study (centre of swath) and Noyes (2005), for the entire AATSR swath, and Dundas (1997), for an unspecified ATSR-1/-2 across track position. For the results of this study, the numbers presented correspond to the rates of change in ΔBT with respect to SDI. The results for each study have been adjusted to a common scale to enable direct comparison between studies (see column #2 for scaling methods used in each case).

Instrument	Scaling method	Experiment	n37 (K)	n11 (K)	n12 (K)	f37 (K)	f11 (K)	f12 (K)
AATSR	Adjusted so that the root sum of the squares across all views/channels is one.	Noyes (2005)	−0.12	−0.31	−0.18	−0.41	−0.68	−0.48
		Haywood (this study)	−0.14	−0.42	−0.27	−0.29	−0.66	−0.46
		OPAC (this study)	−0.16	−0.36	−0.37	−0.31	−0.57	−0.54
AATSR	Normalised at 11 μm across each view to match results of Dundas (1997).	Noyes (2005)	−0.33	−0.83	−0.50	−0.86	−1.43	−1.00
ATSR-1/-2		Dundas (1997)	−0.51	−0.83	−0.80	−0.90	−1.43	−1.37
ATSR-1		Haywood (this study)	−0.28	−0.83	−0.59	−0.67	−1.43	−1.08
		OPAC (this study)	−0.38	−0.83	−0.89	−0.80	−1.43	−1.40

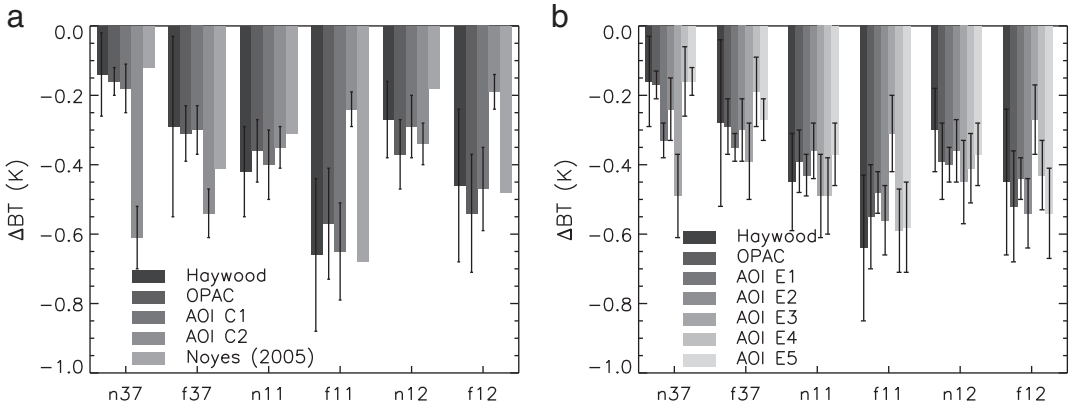

Fig. 5. Comparison of BT deficits for the AATSR centre (a) and edge (b) of swath (also see Table 3). The ΔBTs for each set of results have been scaled such that the root sum of the squares is equal to one. The 'AOI' refer to the areas of interest for which empirical estimates are derived (see Section 3.2).

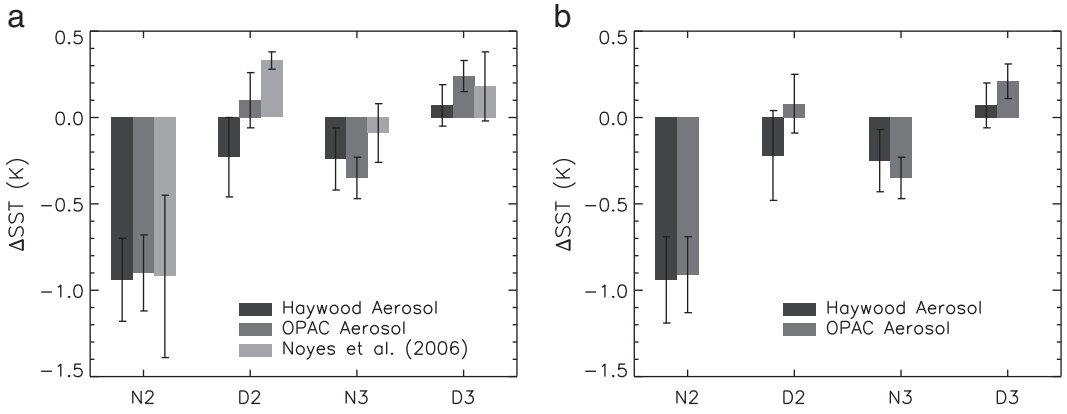

Fig. 6. Comparison of ΔSSTs for the AATSR centre (a) and edge (b) of swath. The results of Noyes et al. (2006) correspond to observations in the Caribbean over the entire AATSR swath. The ΔSSTs for each set of results have been scaled such that the root sum of the squares across all retrievals is equal to one.

SEVIRI SDI data corresponding to ten dates during the 2005 northern hemisphere summer were available for this experiment. Only night time data were considered: firstly, because the SEVIRI SDI can only be calculated directly at night (Section 2.2) and secondly, because the relative effects on all AATSR channels and views need to be examined simultaneously (as has been done for the RTM analysis).

The first step in the analysis was to remove cloudy pixels in both data sets. This was done using the operational cloud mask provided with each data set, extended by one edge pixel to ensure cloud edges were also removed. (Visual inspection of both SEVIRI and ATSR imagery suggests that the operational cloud masks occasionally 'miss' cloud margins.) The remaining cloud-free pixels were then averaged at 0.1° in order to map each data set onto a common grid for the purpose of comparison.

Using the averaged data, small areas of interest (AOIs) within the main study area were tested for significant SDI–BT relationships due to aerosol effects. These areas were restricted to $1\times1°$ in size to minimise the influence of other factors (e.g., water vapour and surface temperature) on the BT and SDI variations. AOIs along each edge and the centre of the AATSR swath were analysed, incrementing each box location by 0.2° along-track (e.g. Fig. 7). The criteria adopted for identifying a significant SDI–BT relationship within an AOI were as follows:

1. At least thirty 0.1° bins are cloud-free and have an SDI of at least 0.2 (this is the value above which SDI confidently indicates the presence of desert dust—see Section 2.2).
2. The standard deviation of the SDI bins (with $SDI \geq 0.2$) is at least 0.1, to ensure some variability due to aerosol.
3. For all channels and views, the BT vs SDI relationship is negative and r is significant at the 5% level (one-tailed distribution). (Positive relationships are likely to be influenced by non-aerosol effects, which are not investigated in this study. For example, under the appropriate atmospheric conditions, an increase in SST or tropospheric temperature may cause a slight increase in SDI and an increase in BT.)

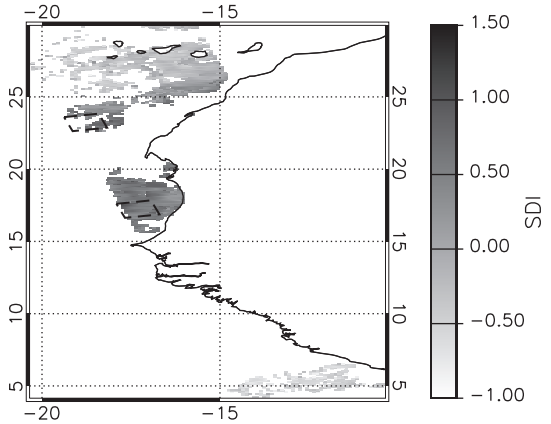

Fig. 7. Example of two empirical AOI test areas shown by the black dashed lines (AOIs correspond to E2 (North) and E3 (South)—see Table 4). The data shown are SDI for 23:00 on 04/08/05 and correspond to AATSR orbit 17933. White space corresponds to cloudy or missing data.

This selection process, right through from cloud screening, to rejection of insignificant BT vs SDI relationships, was achieved through the use of a specially-written Interactive Data Language (IDL) software package that enabled full automation of this process.

3.2.2. Results

Using these selection criteria, several candidate AOIs were identified through the automated AOI selection process described in Section 3.2.1. Where overlapping 1° AOIs met the criteria, the AOI with the overall lowest standard errors of the linear regression fits between the BT and SDI data was selected. (This secondary selection process was performed by hand as the number of AOIs resulting from the automated selection process was small; just two for the centre, and fifteen for the edge of swath.) The overall AOI selection process resulted in just two centre-of-swath and five edge-of-swath AOIs (Table 4, Fig. 7). This is a rather modest number of cases given the amount of data searched, and reflects the fact that many dust-contaminated pixels are screened as cloud (e.g. white areas in Fig. 7).

Comparing the empirical results with those from the modelling demonstrates that in general, the behaviour of the BTs is similar to that predicted by the simulations in this study, and the results of Dundas (1997) and Noyes (2005) (Fig. 5). In most cases, the results agree within the estimated uncertainties. Two exceptions are AOIs C2 and E3, where the inter-channel BT relationships are inconsistent with any other results. In both cases, the results for n37 and f37 are anomalously high, whereas the results for f11 and f12 are anomalously low. This behaviour is likely to be a result of effects other than, or in addition to, Saharan dust and therefore these AOIs are not considered further in this study.

For the other AOIs, the numerical differences between the mean empirical and theoretical ΔBT slopes with SDI are found to be less than 0.1 K in all cases. For the centre of the swath, the slopes of ΔBT with SDI modelled using the Haywood parameters are closest to the equivalent empirical results, with differences for each channel/view ranging between just −0.01 K and 0.03 K. The agreement is still good at the edges of the swath, but in this case, the mean slopes of ΔBT with SDI modelled with the OPAC parameters show the best agreement (−0.01 to 0.01 K for all channels/views except f37, where the difference is 0.06 K). Overall, these results suggest that the capability to model the effects of Saharan dust for the ATSR BTs is adequate for the purposes of this study.

4. Development of the dust index

In Section 3, the effects of aerosol on ATSR BTs were simulated using a radiative transfer model. The accuracy of the simulations was verified by comparing the results with those derived in other ATSR-related studies, and empirical AATSR data analysed in this study. Having determined that the capability to model the effects of dust on ATSR infrared BTs is adequate, the simulations are now used to define an infrared ATSR Saharan dust index, or ASDI.

The basis of the index is that Saharan dust effects on BTs vary with infrared wavelength according to a relatively constant pattern (or 'mode'), while the absolute BT deficits depend on the AOD and height of the aerosol layer. Owing to the means of defining the ASDI, any component of BT variability that reflects the impact of water vapour should not be captured by the index. It is found that the relationship between some channel BT difference (BTD) pairs in 2-D space is distinct and confined to a single axis for clear-sky aerosol-free observations. However, when aerosol is present, a marked change in this relationship is observed and the loci of the data move away from the clear-sky axis. Figs. 8 and 9 illustrate this behaviour for two sets of BTD pairs. In Fig. 8, the BTDs plotted are the clear-sky RTM simulations from Section 3. In both cases, the BTD–BTD relationship is nearly linear and the correlation coefficient, r, is close to one. Fig. 9 shows the corresponding aerosol simulations for the same BTD pairs, with the data points coloured according to their SDI. These data are clearly displaced from the clear-sky relationship from Fig. 8, which is indicated by the solid black lines in the plot. The amount of displacement is dependent on the SDI, where the direction of increasing SDI is approximately orthogonal to the clear-sky line. Empirical AATSR and SEVIRI SDI data plotted in this way also demonstrate this relationship (not shown).

The ASDI is developed using this BTD–BTD relationship and principal component analysis (PCA) to distinguish between the clear-sky BTD behaviour and that of the aerosol-contaminated BTDs. PCA is a linear transformation that converts the data to a new coordinate system such that the first axis (or principal component, PC) represents the greatest degree of variability in the input dataset, the second axis the second largest amount of the remaining variability, third axis the third largest, and so on. The PCA transformation can be considered as a translation (to ensure the data are zero mean) and a rotation to align the data distribution with the coordinate axis. By applying PCA to the clear-sky BTDs, the first PC represents the expected clear-sky variation—i.e. along the solid regression line shown in Fig. 8. As principal components are, by definition, orthogonal, the second PC is effectively the distance from this regression line and represents the BTD changes that we can distinguish from normal clear-sky conditions. The index itself is therefore defined by the second principal component. The application for PCA in this type of analysis was originally identified by Merchant et al. (2006), who used the SEVIRI channels at 3.9, 8.7, 11 and 12 μm to develop a night-time dust index (Section 2.2). For ATSR, we also have the data from the forward view, which introduces the possibility of defining an infrared index that may be used during the day.

Including both forward and nadir views and all three thermal channels, there are 105 unique BTD pairs that can be defined for the

Table 4
Location and overpass information for the AOIs used in the study. Column 'N' indicates the number of cloud-free 0.1° bins in the AOI.

Position	AOI #	Date	SEVIRI slot	AATSR orbit	N	Box corners (first row: °N, second row: °E)			
Centre	C1	20/07/05	01:00	17705	33	29.09	29.31	28.34	28.11
						−44.47	−43.49	−43.27	−44.24
	C2	21/07/05	00:00	17719	31	24.69	24.91	23.94	23.71
						−35.54	−34.56	−34.33	−35.31
Edge	E1	04/08/05	23:00	17933	30	25.78	26.00	25.02	24.81
						−15.73	−14.76	−14.54	−15.52
	E2	04/08/05	23:00	17933	38	23.60	23.84	22.87	22.63
						−19.38	−18.41	−18.17	−19.14
	E3	04/08/05	23:00	17933	91	17.60	17.84	16.87	16.63
						−17.91	−16.94	−16.70	−17.67
	E4	05/09/05	23:00	18391	47	29.00	29.24	28.27	28.03
						−19.27	−18.29	−18.06	−19.03
	E5	05/09/05	23:00	18391	49	26.80	27.04	26.07	25.83
						−18.73	−17.76	−17.52	−18.49

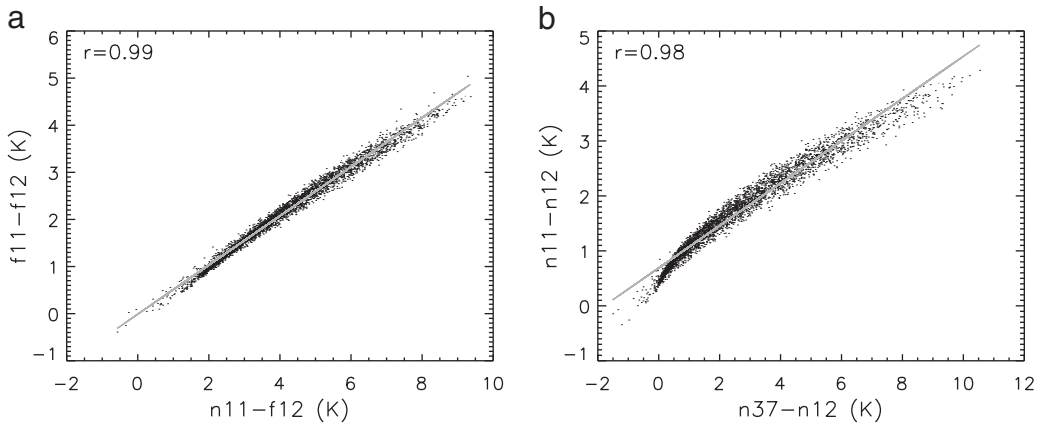

Fig. 8. Variation of simulated clear-sky BTDs in 2D-space for (a) f11–f12 and n11–f12 and (b) the n11–n12 and n37–n21 BTD pairs.

ATSR sensors. Therefore the first task in developing an ASDI is to identify the BTD combination(s) that are most effective for distinguishing between dusty and non-dusty conditions. To do this, a PCA was performed on the simulations for each pair of clear-sky BTDs to determine the coefficients of the first and second principal components. Values for an experimental dust index were then calculated for both the clear-sky and aerosol-contaminated simulations using the coefficients of the second principal component. The properties of this experimental index are tested to establish whether the clear-sky index values are distinct from the aerosol-contaminated index values and how well the index compares with the equivalent simulated SEVIRI SDI. It is also desirable for the clear-sky BTD relationship to be approximately linear, so that the first principal component accounts for as much of the clear-sky variability as possible. Specifically, the results of six tests are used to rate each experimental index/BTD pair:

1. low value of the standard y-error of the linear regression of the clear-sky BTDs
2. low correlation between the first principal component and SDI
3. high correlation between the experimental dust index for the aerosol-contaminated simulations and corresponding SDI
4. low overlap between the distributions of the clear-sky and aerosol-contaminated experimental index values
5. low RMS across all SST retrievals of the mean ΔSSTs for simulations in the overlap zone
6. low RMS across all SST retrievals of the standard deviation of the ΔSSTs for simulations in the overlap zone.

Separate analyses are carried out for both the centre and edges of the swath and for each ATSR instrument. The results of the tests are considered separately for the Haywood and OPAC simulations. Apart from the AATSR edge-of-swath simulations, the f11–f12, n11–f12 BTD pair is consistently rated top for all the ATSRs in the Haywood simulations. For the OPAC simulations, the results are less conclusive, with no consistent top BTD pair across all ATSRs and swath positions. In addition, the correlations between the experimental indices and SDI for the aerosol-contaminated simulations are much lower than for the Haywood simulations. Given these results, the f11–f12, n11–f12 BTD pair is selected to define the ASDI. Using this pair is also a convenient choice as it does not rely on data from the 3.7 μm channel and so can be used both during the day and at night.

We also define a second ASDI that uses nadir-only data for situations where data from the forward view are not available. Differences between pixel availability in the two ATSR views usually occur at cloud edges where one view has been flagged cloudy and the other clear, owing to differences in view geometry (clouds in the forward view may be 'offset' relative to the nadir view). Although this situation does not occur very frequently, investigating a nadir-only index is also useful to prepare for the ATSR follow-on instrument, the Sea and Land Surface Temperature Radiometer (SLSTR), which will not have a forward view at the swath edges.

Only three sets of BTD pairs are nadir-only and none of these rated very highly in the assessment areas. However, the n11–n12, n37–n12 pair was rated as the top nadir-only pair across all the Haywood and OPAC simulations and was therefore chosen as the basis for the

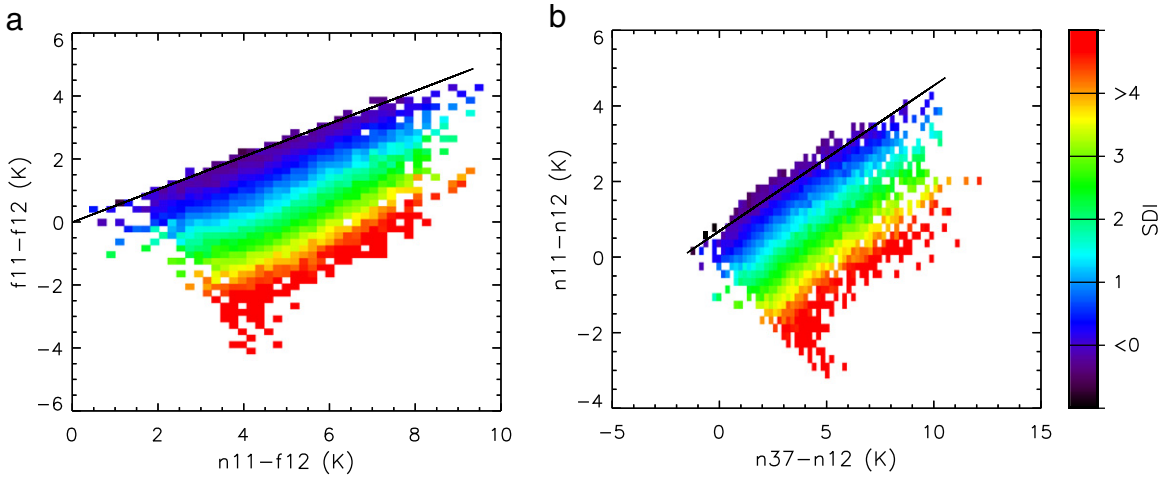

Fig. 9. As for Fig. 8, but for simulations including dust aerosol (Haywood optical properties). The simulations have been binned into 0.2-K BTD 2D bins, where the colour shows the average SDI for that bin. Also shown are the clear-sky regression lines from Fig. 8.

Table 5
Summary of PCA for ASDI2. The coefficients of the derived variables are listed according to their position within a 2 × 2 matrix, Δ, where row 1 corresponds to the first PC and row 2 to the second PC, and column 1 corresponds to the n11–f12 (n37–n12) BTD and column 2 to the f11–f12 (n11–n12) BTD for ASDI2 (ASDI3). The means used to centre the data before performing the PCA are also given in column 'BTD means', where mean (1) corresponds to n11–f12 (n37–n12) and mean (2) to the f11–f12 (n11–n12) BTD for ASDI2 (ASDI3). The mode and standard deviation (Stdev) of the clear-sky distribution are also given (see text). Column 'Yerr' gives the standard error of the fit for the clear-sky BTD relationship (test1). Column 'SDI r^2' gives the coefficient of determination between the SDI and each principal component applied to the aerosol simulations (tests 2 and 3).

Sensor	Swath	Yerr (K)	SDI r^2		Δ (row, column)				BTD means (K)		Mode (K)	Stdev (K)
			PC1	PC2	(1, 1)	(1, 2)	(2, 1)	(2, 2)	(1)	(2)		
AATSR	Centre	0.10	0.00	0.96	−1.692677	−0.884451	0.039603	−0.075793	4.05	2.10	0.025	0.069
	Edge	0.08	0.05	0.95	−1.516518	−0.890740	0.034224	−0.058267	3.55	2.06	0.025	0.046
ATSR2	Centre	0.09	0.00	0.96	−1.650199	−0.828440	0.037019	−0.073739	4.04	2.08	0.025	0.066
	Edge	0.08	0.03	0.95	−1.471430	−0.835477	0.032349	−0.056972	3.53	2.04	0.025	0.044
ATSR1	Centre	0.08	0.02	0.96	−1.518406	−0.696160	0.028547	−0.062264	3.46	1.51	0.025	0.047
	Edge	0.06	0.01	0.95	−1.338954	−0.702483	0.025487	−0.048580	2.97	1.47	0.025	0.033

Table 6
As for Table 5, but for ASDI3.

Sensor	Swath	Yerr (K)	SDI r^2		Δ (row, column)				BTD means (K)		Mode (K)	Stdev (K)
			PC1	PC2	(1, 1)	(1, 2)	(2, 1)	(2, 2)	(1)	(2)		
AATSR	Centre	0.16	0.07	0.97	−2.147758	−0.830669	0.052194	−0.134951	2.53	1.66	−0.025	0.203
	Edge	0.16	0.06	0.98	−2.239538	−0.848934	0.054305	−0.143261	2.64	1.72	−0.025	0.227
ATSR2	Centre	0.15	0.06	0.97	−2.106680	−0.784219	0.050251	−0.134992	2.36	1.64	−0.025	0.202
	Edge	0.16	0.06	0.97	−2.196239	−0.800914	0.052165	−0.143045	2.46	1.69	−0.025	0.225
ATSR1	Centre	0.12	0.11	0.96	−2.007172	−0.652521	0.035862	−0.110313	2.00	1.19	−0.025	0.131
	Edge	0.13	0.14	0.97	−2.097316	−0.668002	0.037268	−0.117009	2.09	1.23	−0.025	0.146

second ASDI. To distinguish between these ASDIs, the two-channel ASDI (f11–f12, n11–f12) is hereafter referred to as ASDI2, and the three-channel ASDI (n11–n12, n37–n12) as ASDI3. The coefficients of the derived variables (Δ) for the PCA carried out for each ATSR instrument are presented in Tables 5 and 6. Following the usual conventions when performing a PCA, each BTD data set has been centred about the mean; these means are also supplied in Tables 5 and 6. (The results of the six tests for each ASDI are given in Tables 5–7). Practically, ASDI2 and ASDI3 are calculated using the coefficients from the second PC according to Eqs. (3) and (4):

$$ASDI2 = 10\left(\Delta_{(2,1).}\left(n11-f12-Mean_{(1)}\right) + \Delta_{(2,2).}\left(f11-f12-Mean_{(2)}\right)\right) \quad (3)$$

$$ASDI3 = 10\left(\Delta_{(2,1).}\left(n37-n12-Mean_{(1)}\right) + \Delta_{(2,2).}\left(n11-n12-Mean_{(2)}\right)\right). \quad (4)$$

A scaling factor of ten is employed simply to make the resulting numbers larger and more manageable, and also to align the ASDI with the SDI scaling. The PCAs for both ASDI2 and ASDI3 yield sufficiently different results between the centre and edges of the swath to justify defining separate coefficients (Coef) and means (Mean). For example, applying the centre-of-swath PCA coefficients to the simulated edge-of-swath BTDs is found to give an ASDI value that may differ from that obtained using the edge-of-swath coefficients by up to 20% of the maximum ASDI. For pixels located between the swath edge and centre, the PCA coefficients and means are interpolated according to air mass factor (where an air mass factor of 1.0 corresponds to a viewing angle of 0°).

Fig. 10 shows the distribution of ASDI2 and ASDI3 for both clear-sky (solid lines) and aerosol-contaminated (dotted lines) simulations for the centre of the AATSR swath. In both cases the aerosol-contaminated distributions are distinct from the clear-sky distributions, where the latter are well approximated by a Gaussian function. There is some overlap between the two distributions for both ASDIs, although the overlap is considerably less for ASDI2 than for ASDI3. Both the histograms and the results of the six assessment tests suggest that ASDI2 should generally perform better than ASDI3 in detecting dust aerosol.

To implement the ASDI in a practical sense, a threshold is defined above which the ASDI is assumed to correspond to a dusty observation where the SST may be biased. Any threshold selection is subjective, but is defined here by considering the mode plus *n* standard deviations of the clear-sky Gaussian function (Tables 5 and 6). A threshold corresponding to three standard deviations is adopted throughout the rest of this study. Table 7 illustrates the impact of varying this threshold, considering the number of 'missed' dusty observations and the effect on the simulated SST bias due to aerosol for those missed data.

Table 7
Impact of changing the ASDI clear-sky threshold. 'N' indicates the number of aerosol-contaminated simulations that fall within the clear-sky limits. ΔSST corresponds to the bias due to aerosol for those simulations. Results are shown for centre of swath simulations.

ASDI	Threshold choice	Value	N	ΔSST mean ± standard deviation (K)			
				N2	D2	N3	D3
ASDI2	Mode + 3 stdev	0.198	157	−0.21 ± 0.39	0.48 ± 0.49	−0.02 ± 0.12	0.26 ± 0.24
	Mode + 2 stdev	0.140	91	−0.12 ± 0.31	0.44 ± 0.50	−0.01 ± 0.12	0.24 ± 0.25
	Mode + 1 stdev	0.083	40	−0.14 ± 0.32	0.29 ± 0.55	0.02 ± 0.11	0.26 ± 0.33
ASDI3	Mode + 3 stdev	0.620	648	−0.93 ± 0.79	0.65 ± 0.34	−0.32 ± 0.35	0.50 ± 0.34
	Mode + 2 stdev	0.405	437	−0.62 ± 0.62	0.69 ± 0.31	−0.23 ± 0.29	0.42 ± 0.32
	Mode + 1 stdev	0.190	237	−0.34 ± 0.48	0.75 ± 0.24	−0.15 ± 0.23	0.33 ± 0.30

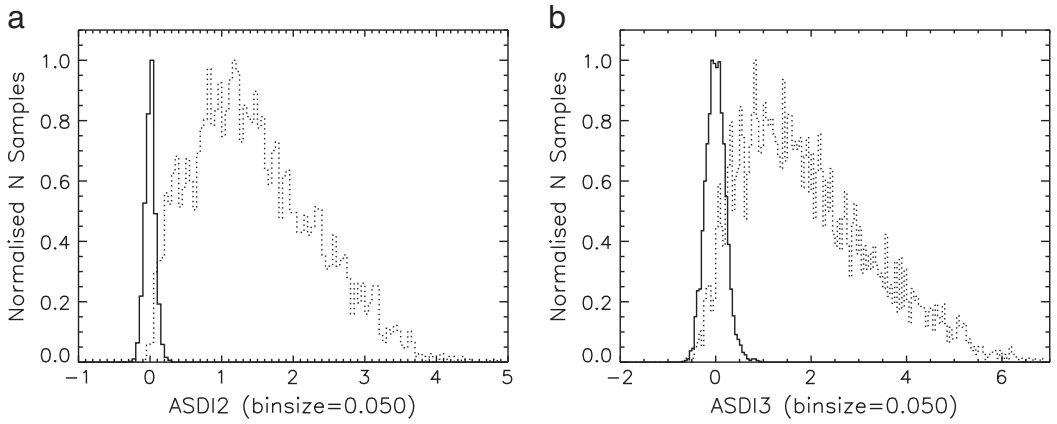

Fig. 10. Histograms of simulated centre-of-swath AATSR (a) ASDI2 and (b) ASDI3 showing both clear-sky (solid line) and dust-contaminated (dotted line) distributions.

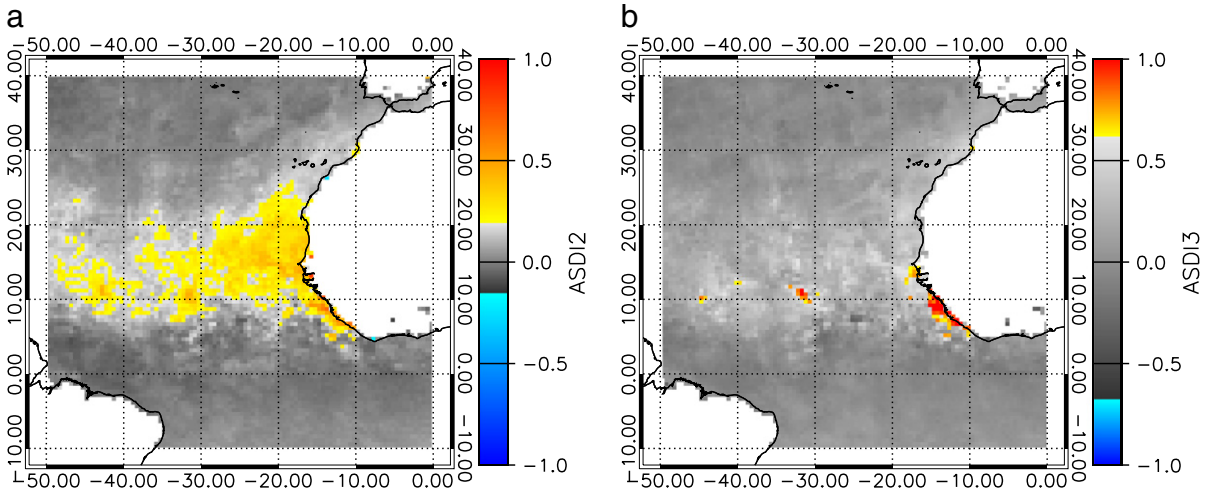

Fig. 11. Composites for June through August 2007 for (a) ASDI2 and (b) ASDI3. Grey scaling indicates grid boxes where the ASDI value falls within the mode ± three standard deviation clear-sky limit adopted in this study.

An empirical example of each ASDI is given in Fig. 11, which shows averaged values over the period June through August 2007, re-sampled to a 0.5° grid. The operational AATSR cloud mask has been employed to remove pixels flagged as cloud for each overpass used (some cloud contamination may remain but the overall effects should be minimal owing to the fact that the data has been averaged over a long period of time). The images clearly show the Saharan dust trail across the Atlantic, highlighted by the elevated values of ASDI. As anticipated from the modelling results, Saharan dust seems to be more readily detected using the ASDI2. ASDI3 values along the Saharan dust trail apparent in the ASDI2 image are elevated, but typically fall within the clear-sky threshold limits. Reducing the ASDI3 threshold results in more dust flagging that matches spatially with the ASDI2, but also leads to an increase in the number of dust-flagged cells that do not match the ASDI2 pattern. These results suggest that ASDI3 is probably only useful in detecting those observations most strongly affected by dust.

Like the SEVIRI SDI, each ASDI is correlated with both AOD and the height of the aerosol layer. Examining the results for all ATSRs and both swath positions, approximately 53% of the variance in each ASDI is accounted for by the change in AOD (correlation coefficient r typically ≈ 0.73), with a further ~24% due to the height of the aerosol layer (r typically ≈ 0.49). The remaining variation in each ASDI is due to other state variables, namely water vapour, atmospheric temperature, SST and the surface–air temperature difference. The correlation coefficient, r, between surface–air temperature difference and water vapour and both ASDIs is always significant (p values are ~0.00) and generally found to be around 0.15 and −0.1, respectively. For SST and the temperature lapse rate, the relationship with each ASDI is less consistent between the ATSRs and the centre and edges of the swath. For these variables, the magnitude of r is generally below 0.05 and is often insignificantly different from zero. (See Table 8 for example values of r and p for the AATSR.)

Table 8
Correlation between ASDI and atmospheric and surface state parameters prescribed in the simulations. Results here are shown for the AATSR centre of swath; similar results are obtained for the edge of the swath and for ATSR-1 and -2.

Swath position	ASDI vs <parameter>	R		P value	
		ASDI2	ASDI3	ASDI2	ASDI3
Centre	AOD	0.73	0.73	0.00	0.00
	Aerosol height	0.49	0.47	0.00	0.00
	SST	−0.01	−0.09	0.50	0.00
	T lapse rate (above 100 Hpa)	−0.03	0.04	0.04	0.01
	Surface–air T difference	0.15	0.16	0.00	0.00
	Precipitable water	−0.10	−0.11	0.00	0.00
Edge	AOD	0.73	0.72	0.00	0.00
	Aerosol height	0.48	0.48	0.00	0.00
	SST	−0.06	−0.04	0.00	0.01
	T Lapse rate (above 100 Hpa)	0.01	−0.01	0.45	0.74
	Surface–air T difference	0.16	0.16	0.00	0.00
	Precipitable water	−0.13	−0.08	0.00	0.00

Table 9
Details of the ATSR-2 imagery used in the experiment. Latitudes and longitudes are approximate and to the nearest degree.

Image no.	ATSR-2 orbit number	Orbit date	Min lat (°N)	Max lat (°N)	Min long (°E)	Max long (°E)
1	01465	01/08/95	27	31	154	160
2	01503	04/08/95	−3	2	−99	−94
3	01506	04/08/95	−48	−41	−164	−156
4	26772	03/06/00	25	32	170	176

5. Dust index evaluation

Having defined a theoretical infrared dust index for the ATSR instruments, we now turn our attention to evaluating the performance of this index when applied to empirical ATSR data. The performance of both ASDI2 and ASDI3 is characterised under dust-free conditions and ASDI2 values are evaluated against independent visible AOD data (ASDI3 can only be implemented at night). The behaviour of both ASDIs over cloudy pixels is also investigated.

5.1. Evaluation in dust-free conditions

In Section 4, theoretical clear-sky distributions of ASDI were constructed, which were found to be well approximated by a Gaussian function. These distributions were used to define thresholds for ASDI; values above these thresholds are assumed to correspond to dust-contaminated observations, whilst values below are considered dust-free. To test the validity of these theoretical results, the ASDI algorithms are applied to ATSR data where the presence of mineral dust aerosol is unlikely. The observed distributions are then compared with the theoretical equivalents.

Both ATSR-2 and AATSR imagery are used here. The ATSR-2 data consist of four dust-free night time images that have been cloud screened by hand (Table 9—the hand cloud masks were provided courtesy of C. Old, now at University of Bangor). The AATSR data correspond to overpasses for the Pacific Ocean between −20 and −15°N latitude, and −160 and −150°E longitude during January 2005 (day and night). This geographical and temporal study regime was selected on the basis that aerosol loading should be low, as determined from Moderate Resolution Imaging Spectroradiometer (MODIS) aerosol data 'quick look' images (http://modis-atmos.gsfc.nasa.gov/IMAGES/mod08m_menu.html).

Fig. 12 shows the ASDI retrievals and corresponding hand cloud masks for ATSR-2 image 1. Histograms of the ASDI distributions are shown separately for clear-sky and cloudy pixels in Fig. 13. The results demonstrate that the observed values of ASDI over clear sky are typically within the theoretical limits and the distribution is approximately Gaussian. ASDI values for cloudy pixels are generally outside these limits: ASDI2 in particular seems to be very effective in detecting cloudy pixels, with values falling both above and below the clear-sky range. The lower ASDI2 values tend to occur on the leading

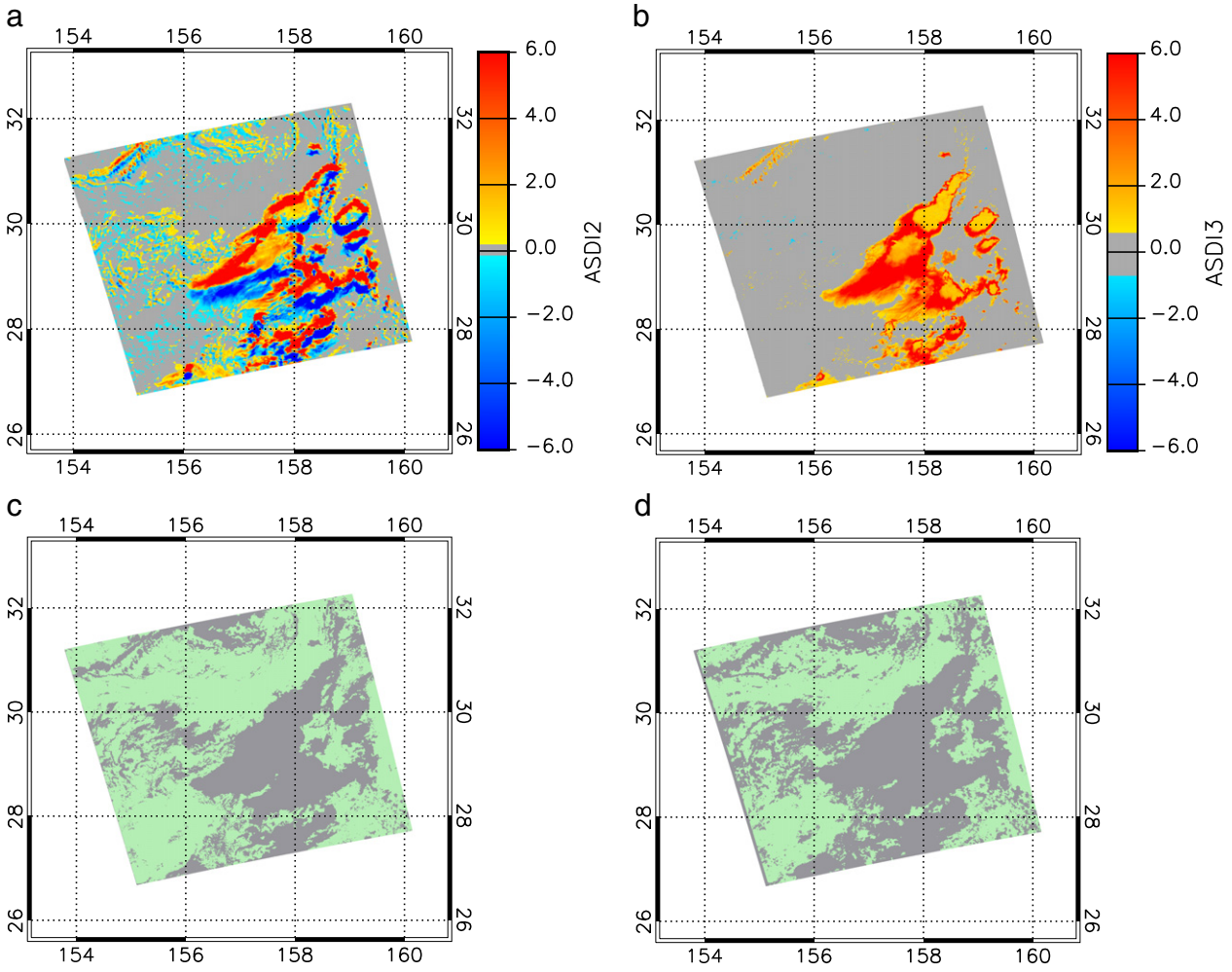

Fig. 12. ASDI2 (a) and ASDI3 (b) retrievals, together with the associated hand-screened nadir (c) and forward (d) cloud masks corresponding to the ATSR-2 orbit 01465 (image 1). In the ASDI images, the grey colour indicates the theoretical clear-sky ASDI limits. In the cloud mask images green indicates cloud-free and grey, cloudy pixels.

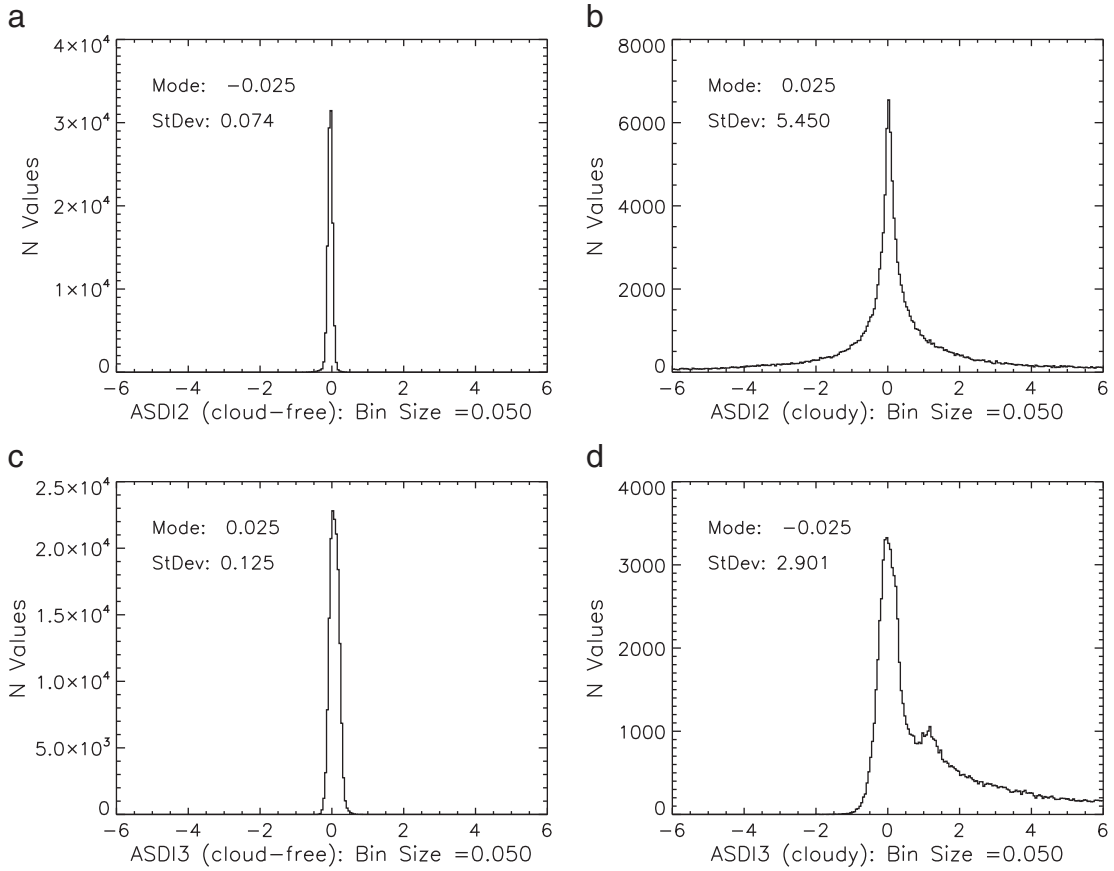

Fig. 13. ASDI distributions corresponding to Fig. 12. (a) and (c) show the clear-sky distributions for ASDI2 and ASDI3, respectively, where (b) and (d) show the equivalent cloudy ASDI distributions.

edge of the cloud (these are ascending node images), which is an artefact of the difference in the cloud-viewing geometry between the nadir and forward views. This effect is not seen in the ASDI3 retrievals, which uses only the nadir view, and nearly all of the cloudy pixels have ASDI3 values above the theoretical clear-sky range. The results presented here suggest that a further use of both ASDIs could be to identify cloud that may have by-passed previous cloud screening efforts in the data, i.e. 'cloud contamination'. For example, values of ASDI2 below the theoretical clear-sky limits could be used to indicate the presence of cloud as this range of ASDI2 does not appear to correspond to either dust or clear-sky conditions.

Similar results are obtained for the other ATSR-2, and AATSR images. Summaries of the clear-sky distributions for each image are illustrated in Figs. 14 and 15. The distributions match well with the theoretical distributions, particularly for the hand-cloud-screened ATSR-2 images, which reflect the more accurate cloud masks used in this analysis. The operational ATSR cloud mask scheme works well, but does not detect every cloudy pixel (Merchant et al., 2005; Noyes et al., 2006), resulting in the observed broadening of the ASDI distributions for the AATSR data.

5.2. Evaluation with other independent aerosol data

Having established that the empirical clear-sky ASDI distributions agree well with those defined theoretically, the performance of the ASDI in dusty conditions is now assessed. Evaluation is carried out using three independent visible AOD aerosol data sets. While ASDI is not a direct measure of AOD, the theoretical analysis performed previously suggests there is a strong relationship with 10 μm AOD, so we might also anticipate some relationship with visible AOD. The work of Merchant et al. (2006) supports this, and they report a correlation coefficient of 0.34 between MODIS AOD at 0.55 μm and SEVIRI SDI. Considering this predicted correspondence, temporally and spatially collocated ASDI2 and visible AOD data are also compared in this study. ASDI3 data are not analysed in this way as this index requires the ATSR 3.7 μm channel, which is unreliable during the day due to contamination from reflected solar radiation (which has not been included in the modelling done in this study).

The visible AOD data used in this study comprise of:

1. MODIS/Terra 0.55 μm AOD, 10 km spatial resolution (product MOD04, see Remer et al., 2009 and Tanré et al., 1997)
2. AATSR visible AOD, 10 km spatial resolution (Grey et al., 2006; data supplied by private communication)
3. AErosol RObotic NETwork (AERONET) visible AOD, point observations (e.g. Holben et al., 1998).

For the comparisons with MODIS and AATSR visible AOD, the data were compared over several dates during 2005 for overpasses crossing the main study area in the Atlantic Ocean. In each case, both the ASDI2 and AOD data were re-gridded to 0.25° to enable the data sets to be correlated. For the AATSR data, the temporal and spatial match is exact, since the ASDI2 retrievals were performed for the same orbits. For the comparisons with MODIS, overpasses within 1 h of the AATSR overpass were used. In both cases, cloud-contaminated observations were identified and rejected using the operational cloud masks provided with the datasets.

Tables 10 and 11 summarise the comparisons. In each case, a 'dust fraction' (D.F.) has been calculated that indicates the percentage of grid cells where the ASDI2 is above the theoretical clear-sky limit (0.198). This parameter should provide some indication of the abundance of dust in the imagery. Correlation coefficients are presented for all matched grid cells, and for 'dusty' grid cells, where

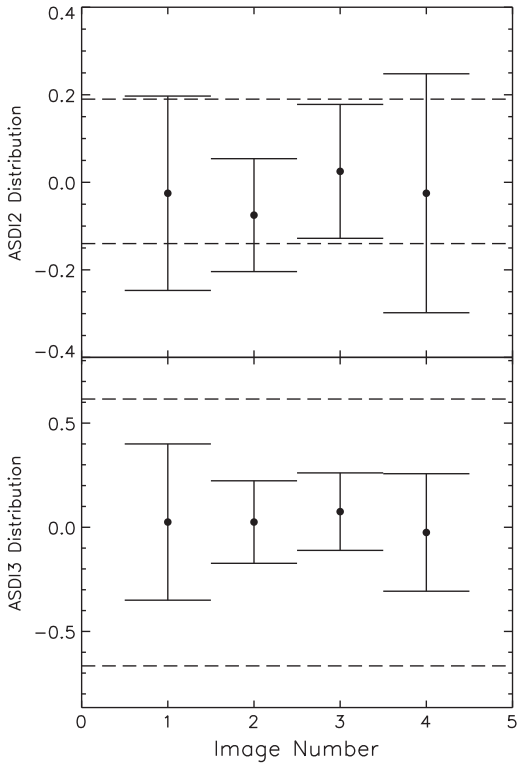

Fig. 14. ASDI distributions for clear-sky ATSR-2 imagery (Table 9. Also see Figs. 11 and 12). Filled circles represent the modes of the distributions, while the whiskers correspond to three standard deviations. The dashed lines represent the theoretical modes ± 3 standard deviations from Tables 5 and 6 (for the standard deviation, the means of the swath centre and edge values have been used).

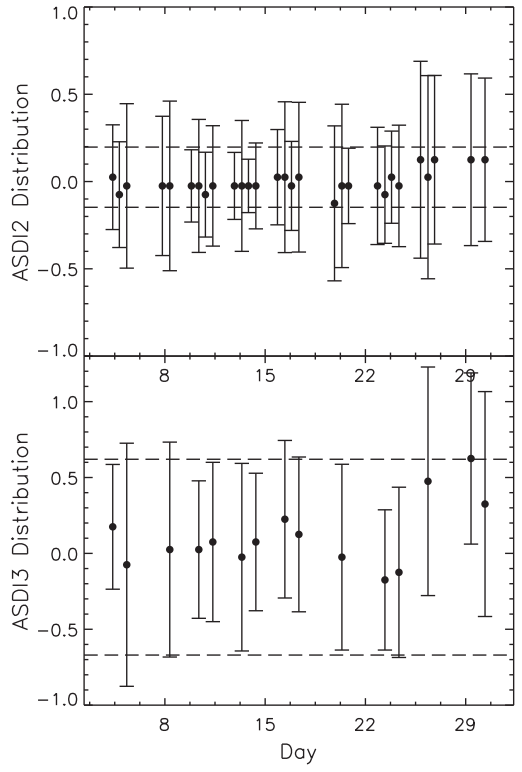

Fig. 15. As for Fig. 14 but for clear-sky AATSR imagery.

Table 10
Comparison between ASDI2 and MODIS AOD at 550 nm for the MODIS 'best' solution, and for MODIS retrievals that use only a dust model (see text). 'Dusty grid cells' refers to correlations performed for grid cells with AOD>0.2 and ASDI2>0.198 (mode + three standard deviations—see Tables 5 and 7). D.F. indicates the % of matched cloud-free grid cells where the ASDI2 is above 0.198. 'r' correlation coefficients in parentheses are where the correlation is not significant at the 5% level (one-tailed test). Correlations are only given for comparisons with ten or more matched grid cells. Both data sets have been averaged to 0.25°.

AATSR overpass		D.F. (%)	All grid cells				Dusty grid cells			
Date	Orbit #		Best		Dust model		Best		Dust model	
			N	r	N	r	N	r	N	r
05/09/05	18384	80.0	80	0.63	45	0.93	64	0.46	27	0.7
04/09/05	18370	31.6	564	0.78	55	(0.20)	175	0.38	0	–
19/06/05	17267	31.0	187	0.96	6	–	58	0.93	0	–
04/10/05	18799	12.2	690	0.64	66	0.53	84	0.34	3	–
03/08/05	17912	9.4	235	0.57	7	–	22	(0.11)	0	–
04/08/05	17926	6.9	29	0.57	2	–	1	–	0	–
19/06/05	17268	4.2	672	0.70	49	(0.15)	23	(−0.03)	0	–
05/10/05	18814	3.6	56	(0.11)	24	(0.38)	0	–	0	–
05/09/05	18385	3.0	33	0.38	3	–	1	–	0	–
04/10/05	18800	2.6	567	0.24	258	(0.05)	11	(0.38)	0	–

the visible AOD is greater than 0.2 and ASDI2 is greater than 0.198. For the MODIS comparisons, two sets of results are presented. MODIS aerosol retrievals assume that both a fine and coarse aerosol mode are present, and the product provides information on which aerosol models have been used for each mode to achieve the final AOD solution (e.g. choice is from three types of marine or two types of dust for the coarse mode; see Remer et al., 2009 for further information). The results given here correspond to the 'best' MODIS AOD solution, which is based on a combination of both fine and coarse aerosol modes using any aerosol model, and the AOD determined for just the coarse aerosol mode where one of the two dust models have been used. Equivalent results for the AATSR visible AOD are not presented as this information is not available in the data products.

In general, the correlation is quite high and nearly always significant at the 5% level (one-tailed test). The results are generally better for overpasses with higher dust fractions. Results for the AATSR AOD comparisons are typically better than for the MODIS AOD, which is probably due to the better temporal and spatial agreement between the AATSR data sets (there are more matched grid cells). Overall, the results are extremely encouraging. Some discrepancies are to be expected given that the visible AOD data will sometimes detect

Table 11
As for Table 10 but showing comparisons between ASDI2 and AATSR AOD.

Overpass		D.F. (%)	All grid cells		Dusty grid cells	
Date	Orbit #		N	r	N	r
20/07/05	17711	67.0	91	0.87	60	0.63
02/08/05	17898	57.5	306	0.91	176	0.79
05/09/05	18384	51.2	244	0.87	120	0.68
18/06/05	17253	41.2	570	0.81	235	0.81
04/08/05	17926	36.3	306	0.94	111	0.92
04/10/05	18799	20.7	523	0.81	108	(0.17)
04/08/05	17927	14.8	183	0.95	27	0.74
18/06/05	17254	13.8	421	0.91	58	0.52
19/06/05	17267	8.6	116	(0.12)	10	0.98
04/10/05	18800	7.5	544	0.46	37	(0.28)
04/08/05	18370	6.5	186	0.54	12	0.79
03/08/05	17912	5.6	143	0.65	8	–
13/12/05	19802	3.4	587	0.10	0	–
19/06/05	17268	2.8	354	0.55	9	–
05/10/05	18814	1.4	345	0.64	4	–
05/09/05	18385	0.8	236	0.41	2	–
20/07/05	17712	0.0	509	(0.07)	0	–
12/12/05	19787	0.0	544	0.12	0	–

aerosols that have little effect at infrared wavelengths, such as biomass burning. However, there are some results that are inconsistent between the two sets of comparisons. For example, the value of r for orbit 17267 is 0.96 for the comparison with MODIS, but only 0.12 for the AATSR AOD comparison. These inconsistencies may be due to differences in the available grid cells used in the comparisons, resulting from orbit path differences and/or differences in cloud masking between AATSR and MODIS, or to errors within the AOD and/or ASDI data sets. For example, Bevan et al. (in press) have compared AATSR AOD data with AERONET in this ocean region and report errors of approximately 0.05 in the satellite 0.55 μm AOD data.

The comparisons with the MODIS dust AOD are poor. With the exception of two AATSR orbits, 18384 and 18799, the correlations are low and insignificant at the 5% level. This result initially appears surprising given that the ASDI has been correlated with a visible AOD that should correspond only to dust. However, by comparing against the MODIS dust AODs we are excluding the clear-sky cases (which are likely to be classified as marine aerosol with low AOD) and selecting just the cases with higher AOD. This can reduce the correlation between ASDI and AOD as the ASDI is more sensitive to the aerosol height for higher AODs. Furthermore, the number of matches is much lower for the 'dust' comparisons and further inspection of the MODIS product indicates that the majority (47–93% with an average over the 10 orbits of 77%) of retrievals use a marine aerosol model for the coarse mode. Repeating the analysis for the coarse mode AOD using any of the marine or dust models results in correlations that are almost identical to those for the MODIS 'best' solution (not shown). These results suggest that the ASDI is also sensitive to marine aerosols in addition to dust. Simulations of marine aerosol showed that it would cause an increase in ASDI, but not sufficient to be distinguishable from normal clear-sky variability.

A slightly different approach is required for comparing the ASDI2 with observations from AERONET. Two AERONET stations have been used in this experiment: Dakar, Senegal (14.394°N, 16.959°W), and Cape Verde (16.733°N, 22.935°W). As both stations are on land, ASDI2 data averaged over a 0.5° box located offshore from each station is used in the comparison. For Dakar, this box ranges between 14.094 and 14.594°N, and 17.659 and 17.159°W. For Cape Verde, an area between 16.483 and 16.983°N, and 22.835 and 22.335°W is used. Two years of data between May 2004 and April 2006 have been analysed in each case, and an average of all available AERONET observations within ±30 min of the AATSR overpass time have been used in the comparison.

Owing to cloud contamination and the incomplete coverage of the AERONET level 2.0 product used here, the number of matchups is quite low. Nevertheless, the results clearly demonstrate a strong correlation between ASDI2 and AOD (Table 12, Fig. 16). Together with

Table 12
Correlation between ASDI2 and AERONET observations. 'All' refers to where all available matches have been included in the correlation; 'Dusty' refers to correlations using only matches where the AOD>0.2 and ASDI2>0.198. 'r' correlation values in parentheses are where the correlation is not significant at the 5% level (one-tailed test).

AERONET wavelength (μm)	Dakar				Cape Verde			
	All		Dusty		All		Dusty	
	N	r	N	r	N	r	N	r
1640	No data				11	0.86	4	(0.60)
1020	29	0.81	8	0.91	11	0.85	4	(0.60)
870	29	0.81	8	0.91	11	0.84	4	(0.59)
675	29	0.80	8	0.91	11	0.83	4	(0.59)
500	No data				11	0.83	4	(0.61)
440	29	0.74	8	0.89	11	0.82	4	(0.60)
380	No data				11	0.82	4	(0.61)
340	No data				11	0.84	4	(0.66)

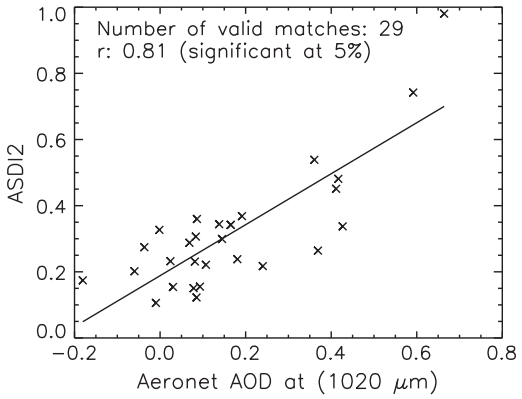

Fig. 16. Comparison between ASDI2 and 1020 μm AOD observed at the Dakar AERONET site.

the results of the MODIS and AATSR visible AOD comparisons, the analysis presented here suggests that the ASDI2 is performing well, with the correlation with AOD being similar to that predicted by the modelling results ($r = 0.73$).

6. Conclusions

Tropospheric mineral dust has been found to cause significant biases (>0.1 K) in ATSR SST retrievals, particularly in the tropical Atlantic Ocean and Mediterranean and Red Seas, where Saharan dust outbreaks occur frequently. In this paper, we have defined the ATSR Saharan Dust Index, or ASDI, which can be used to identify dust-contaminated pixels that may be biased in terms of SST. The primary index, ASDI2, uses only the 11 and 12 μm channels, and therefore provides a consistent means of identifying dust both during the day and at night. The index makes use of the unique dual-view aspect of the ATSR instruments, using data from both the forward and nadir passes. A secondary index, ASDI3 is also defined for situations where the ATSR forward view is not available. This secondary index is less effective than ASDI2 at identifying dust, detecting only the most heavily dust-contaminated observations. Moreover, as this index requires data from the 3.7 μm channel, it can only be used reliably at night.

The definition of the ASDI is based on the work of Merchant et al. (2006), who developed a Saharan Dust Index (SDI) for SEVIRI. It makes use of the variability of BT differences (BTDs) in two-dimensional space (i.e. BTD vs BTD), which is found to differ distinctly between clear-sky and aerosol-contaminated conditions. ASDI2 is based on the f11–f12 and n11–f12 BTDs, while ASDI3 utilises the n11–n12 and n37–n12 BTDs. Following the heritage of the ATSR SST retrieval scheme, the ASDI algorithm is formulated using radiative transfer model simulations for both dusty and non-dusty conditions. We have verified each stage of the development process using empirical data where possible. This is particularly important as the radiative transfer simulations for dusty conditions rely on aerosol properties that may have a high degree of uncertainty. In the final stage of development, ASDI2 has been evaluated using three independent visible AOD data sets from AATSR, MODIS and AERONET. In each case, ASDI2 is well correlated with AOD (r is typically >0.7). This is supported by the theoretical analysis carried out in this study, which also indicates that ASDI is sensitive to the height of the aerosol layer ($r \approx 0.49$).

The ASDI algorithms will be used to identify dust-contaminated ATSR observations within the framework of the ARC project, which aims to produce a long-term, consistent and accurate SST data sets for climate studies. This index will be used to flag ARC SST retrievals that may be biased by the presence of dust. The formulation of both ASDI2 and ASDI3 is such that they may be applied to the entire ATSR record

from 1991 (although it should be noted that we have not assessed the performance on ATSR-1 data under the stratospheric aerosol conditions following the Pinatubo eruption—this will be the subject of future work). Although the focus of this article has been on Saharan dust outflow over the Atlantic Ocean, we expect the ASDI to work well in other dust-affected regions. A preliminary examination at ASDI values in other areas support this inference; however, a more detailed analysis will be carried out in the future to confirm this. Future work will also include a more in-depth look at the effect of the ATSR viewing geometry on the ASDI2. Co-registration of the ATSR nadir and forward views is a known issue, particularly for the latter part of the ATSR-2 record, which may introduce uncertainty into this dual-view dust index where the dust has a heterogeneous spatial distribution. Similarly, uncertainties due to the parallax effect (i.e. dependency of apparent horizontal location of dust due to a combination of view angle and dust layer height/thickness) will also be investigated.

Eventually, it is hoped that the work carried out in this study will also lead to the development of a dust-robust SST retrieval scheme for the ATSR. A further extension could be to develop an ASDI3-type algorithm for other imaging radiometers used for SST retrieval, such as MODIS and AVHRR.

Acknowledgements

This work was carried out within the framework of the ARC project, which is funded jointly by the UK's Natural Environment Research Council (NERC), Ministry of Defence (Joint Grant Scheme), and the Department of Environment, Food and Rural Affairs/Department of Energy and Climate Change (DECC). E.J. Good is now funded at the Met Office by the Joint DECC, Defra and MoD Integrated Climate Programme—GA01101, CBC/2B/0417_Annex C5. The ATSR data used in this study were obtained from the NERC Earth Observation Data Centre (NEODC). The SEVIRI data were provided by the Meteo-France group within EUMETSAT's Ocean and Sea Ice Satellite Application Facility (OSI SAF). The AATSR AOD data were provided by the University of Swansea (courtesy of W. Grey), and were developed as part of the NERC's Climate and Land Surface Systems Interactions Centre (CLASSIC) programme. The MODIS AOD data were provided by NASA. We thank the AERONET principal investigators and their staff for establishing and maintaining the Dakar and Cape Verde AERONET sites used in this investigation. We are also grateful to Chris Old, formerly of the University of Edinburgh, for provision of the hand-screened ATSR-2 cloud masks used in this study.

References

Bevan, S. L., North, P. R. J., Los, S. O., & Grey, W. M. F. (in press). A global dataset of atmospheric aerosol optical depth and surface reflectance from AATSR. *Remote Sensing of Environment*. doi:10.1016/j.rse.2011.05.024.

Brindley, H. E., & Ignatov, A. (2006). Retrieval of mineral aerosol optical depth and size information from Meteosat Second Generation SEVIRI solar reflectance bands. *Remote Sensing of Environment*, *102*, 344–363.

Brindley, H. E., & Russell, J. E. (2006). Improving GERB scene identification using SEVIRI: Infrared dust detection strategy. *Remote Sensing of Environment*, *104*, 426–446.

Brisson, A., Le Borgne, P., & Marsouin, A. (1998). Development of algorithms for SST retrieval at O&SI SAF low and mid latitudes. *CMS report to EUMETSAT, Météo-France/CMS 22302 Lannion, France*.

Carlson, T. N., & Prospero, J. M. (1972). The large-scale movement of saharan air outbreaks over the northern equatorial Atlantic. *Journal of Applied Meteorology*, *11*, 283–297.

Corlett, G. K. (2009). ATSR validation activities: Validation issues report. *Contract report for Space ConneXions Contract 2004-03001/CPEG10*.

Corlett, G. K., Barton, I. J., Donlon, C. J., Edwards, M. C., Good, S. A., Horrocks, L. A., Llewellyn-Jones, D. T., Merchant, C. J., Minnett, P. J., Nightingale, T. J., Noyes, E. J., O'Carroll, A. G., Remedios, J. J., Robinson, I. S., Saunders, R. W., & Watts, J. G. (2006). The accuracy of SST retrievals from AATSR: An initial assessment through geophysical validation against in situ radiometers, buoys and other SST data sets. *Advances in Space Research*, *37*(4), 764–769.

Donlon, C. J., & Robinson, I. S. (1998). Radiometric validation of ERS-1 along-track scanning radiometer average sea surface temperature in the Atlantic Ocean. *Journal of Atmospheric and Oceanic Technology*, *15*(3), 647–660.

Dundas, R. M. (1997). The use of ATSR data to measure the radiative properties of aerosol particles, PhD thesis, University of Leicester.

European Space Agency (2002). *The AATSR products user guide.*

Grey, W. M. F., North, P. R. J., & Los, S. O. (2006). Computationally efficient method for retrieving aerosol optical depth from ATSR-2 and AATSR data. *Applied Optics*, *45*(12), 2786–2795.

Hess, M., Koepke, P., & Schult, I. (1998). Optical properties of aerosols and clouds: The software package OPAC. *Bulletin of the American Meteorological Society*, *79*, 831–844.

Highwood, E. J., Haywood, J. M., Silverstone, M. D., Newman, S. M., & Taylor, J. P. (2003). Radiative properties and direct effect of Saharan dust measured by the C-130 aircraft during Saharan Dust Experiment (SHADE): 2. Terrestrial spectrum. *Journal of Geophysical Research*, *108*(D18), 8578. doi:10.1029/2002JD002552

Holben, B. N., Eck, T. F., Slutsker, I., Tanre, D., Buis, J. P., Setzer, A., Vermote, E., Reagan, J. A., Kaufman, Y., Nakajima, T., Lavenu, F., Jankowiak, I., & Smirnov, A. (1998). AERONET—A federated instrument network and data archive for aerosol characterization. *Remote Sensing of Environment*, *66*, 1–16.

Kilpatrick, K. A., Podesta, G. P., & Evans, R. (2001). Overview of the NOAA/NASA Advanced Very High Resolution Radiometer Pathfinder algorithm for sea surface temperature and associated matchup database. *Journal of Geophysical Research-Oceans*, *106*(C5), 9179–9197.

Llewellyn-Jones, D., Edwards, M. C., Mutlow, C. T., Birks, A. R., Barton, I. J., & Tait, H. (2001). AATSR: Global-change and surface-temperature measurements from Envisat. *ESA Bulletin February*, *2001*(105), 11–21.

Mason, G. (1991). Test and calibration of the Along Track Scanning Radiometer, a satellite-borne infrared radiometer designed to measure sea surface temperature. PhD thesis, University of Oxford.

Merchant, C. J., Embury, O., Le Borgne, P., & Bellec, B. (2006). Saharan dust in night time thermal imagery: Detection and reduction of related biases in retrieved sea surface temperature. *Remote Sensing of Environment*, *104*(1), 15–30.

Merchant, C. J., Harris, A. R., Maturi, E., & MacCallum, S. (2005). Probabilistic physically based cloud screening of satellite infrared imagery for operational sea surface temperature retrieval. *Quarterly Journal of the Royal Meteorological Society*, *131*, 2735–2755.

Merchant, C. J., Harris, A. R., Murray, M. J., & Závody, A. M. (1999). Toward the elimination of bias in satellite retrievals of sea surface temperature 1. Theory, modeling and interalgorithm comparison. *Journal of Geophysical Research*, *104*(C10), 23565–23578. doi:10.1029/1999JC900105

Merchant, C. J., Llewellyn-Jones, D., Saunders, R. W., Rayner, N. A., Kent, E. C., Old, C. P., Berry, D., Birks, A. R., Blackmore, T., Corlett, G. K., Embury, O., Jay, V. L., Kennedy, J., Mutlow, C. T., Nightingale, T. J., O'Carroll, A. G., Pritchard, M. J., Remedios, J. J., & Tett, S. (2008). Deriving a sea surface temperature record suitable for climate change research from the along-track scanning radiometers. *Advances in Space Research*, *41*, 1–11.

Nightingale, T. J., & Birks, A. R. (2004). AATSR algorithm verification: Comparison of AATSR and ATSR-2 data. *AATSR Technical Note*. : Rutherford Appleton Laboratory.

Noyes, E. J. (2005). An investigation into the accuracy of surface temperature retrievals from the AATSR, PhD thesis, University of Leicester.

Noyes, E. J., Minnett, P. J., Remedios, J. J., Corlett, G. K., Good, S. A., & Llewellyn-Jones, D. T. (2006). The accuracy of the AATSR sea surface temperatures in the Caribbean. *Remote Sensing of Environment*, *101*(1), 38–51.

O'Carroll, A. G., Watts, J. G., Horrocks, L. A., Saunders, R. W., & Rayner, N. A. (2006). Validation of the AATSR meteo product sea surface temperature. *Journal of Atmospheric and Oceanic Technology*, *23*(5), 711–726.

O'Carroll, A. G., Eyre, J. R., & Saunders, R. W. (2008). Three-way error analysis between AATSR, AMSR-E and in situ sea surface temperature observations. *Journal of Atmospheric and Oceanic Technology*, *25*(7), 1197–1207.

Pierangelo, C., Chédin, A., Heilliette, S., Jacquinet-Husson, N., & Armante, R. (2004). Dust altitude and infrared optical depth from AIRS. *Atmospheric Chemistry and Phyiscs Discussions*, *4*, 3333–3358.

Prospero, J., & Carlson, T. (1972). Vertical and aerial distribution of Saharan dust over the western equatorial North Atlantic Ocean. *Journal of Geophysical Research*, *77*, 5225–5265.

Remer, L. A., Tanré, D., & Kaufman, Y. J. (2009). *Algorithm for remote sensing of tropospheric aerosol from MODIS: Collection 005, Revision 2, Product ID: MOD04/MYD04.*

Saunders, R. W., Matricardi, M., & Bruenl, P. (1999). An improved fast radiative transfer model for assimilation of satellite radiance observations. *Quarterly Journal of the Royal Meteorological Society*, *125*, 1407–1425.

Saunders, R., & Pascal, B. (2005). RTTOV_8_7 users guide. *EUMETSAT, NWP SAF report*.

Smith, D. L. (2007). Effect of long wavelength response in AATSR filters on brightness temperature measurements. *AATSR Technical Note, PO-TN-RAL-AT-0541, Issue 1.0*. Rutherford Appleton Laboratory.

Smith, D. L., Delderfield, J., Drummond, D., Edwards, T., Mutlow, C. T., Read, P. D., & Toplis, G. M. (2001). Calibration of the AATSR instrument. *Advances in Space Research*, *28*(1), 31–39.

Stamnes, K., Tsay, S. -C., Wiscombe, W., & Jayaweera, K. (1988). Numerically stable algorithm for discrete-ordinate-method radiative transfer in multiple scattering and emitting layered media. *Applied Optics*, *27*(12), 2502–2509.

Tanré, D., Kaufman, Y. J., Herman, M., & Mattoo, S. (1997). Remote sensing of aerosol properties over oceans using the MODIS/EOS spectral radiances. *Journal of Geophysical Research*, *102*(D14), 16971–16988.

Thomas, G. E., Carboni, E., Sayer, A. M., Poulsen, C. A., Siddans, R., & Grainger, R. G. (2009). Oxford-RAL Aerosol and Cloud (ORAC): Aerosol retrievals from satellite radiometers. In A. A. Kokhanovsky, & G. de Leeuw (Eds.), *Satellite aerosol remote sensing over land* (pp. 193–225). Springer-Praxis Books.

Thomas, G. E., Dean, S. M., Carboni, E., Grainger, R. G., Poulsen, C. A., Siddans, R., & Kerridge, B. J. (2007). An optimal estimation aerosol retrieval scheme for (A)ATSR. *Atmospheric, Oceanic and Planetary Physics Technical Memorandum, University of Oxford*. http://www.atm.ox.ac.uk/main/Science/technical.html

Vazquez-Cuervo, J., Armstrong, E. M., & Harris, A. (2004). The effect of aerosols and clouds on the retrieval of infrared sea surface temperature. *Journal of Climate*, *17* (20), 3,921–3,933.

Veefkind, J. P., & de Leeuw, G. (1998). A new algorithm to determine the spectral aerosol optical depth from satellite radiometer measurements. *Journal of Aerosol Science*, *29*, 1237–1248.

Závody, A. M., Mutlow, C. T., & Llewellyn-Jones, D. T. (1995). A radiative transfer model for sea surface temperature retrieval for the along-track scanning radiometer. *Journal of Geophysical Research*, *100*, 937–952.